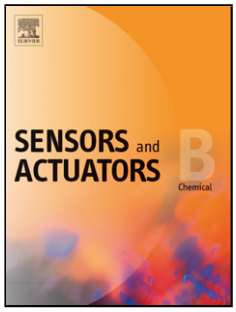

Title: Large-scale controlled bio-inspired fabrication of 3D CeO_2:Eu^{3+} hierarchical structures for evaluation of highly sensitive visualization of latent fingerprints

Authors: N.H. Deepthi, G.P. Darshan, R.B. Basavaraj, B. Daruka Prasad, H. Nagabhushana

PII: S0925-4005(17)31804-X
DOI: http://dx.doi.org/10.1016/j.snb.2017.09.138
Reference: SNB 23229

To appear in: *Sensors and Actuators B*

Received date: 7-6-2017
Revised date: 18-9-2017
Accepted date: 20-9-2017

Please cite this article as: N.H.Deepthi, G.P.Darshan, R.B.Basavaraj, B.Daruka Prasad, H.Nagabhushana, Large-scale controlled bio-inspired fabrication of 3D CeO2:Eu3+ hierarchical structures for evaluation of highly sensitive visualization of latent fingerprints, Sensors and Actuators B: Chemicalhttp://dx.doi.org/10.1016/j.snb.2017.09.138

Large-scale controlled bio-inspired fabrication of 3D $CeO_2:Eu^{3+}$ hierarchical structures for evaluation of highly sensitive visualization of latent fingerprints

N.H. Deepthi[1], G.P. Darshan[2], R.B. Basavaraj[1], B. Daruka Prasad[3], H. Nagabhushana[1,*]

[1]*Prof. C.N. R. Rao Center for Advanced Materials, Tumkur University, Tumkur 572103, India*

[2]*Department of Physics, Acharya Institute of Graduate Studies, Bangalore 560107, India*

[3]*Department of Physics, B.M.S. Institute of Technology and Management, Visveswaraya Technological University affiliated, Bangalore 560064, India*

* Corresponding author: +91- 9945954010, E-mail address: bhushanvlc@gmail.com (H. Nagabhushana).

Graphical abstract

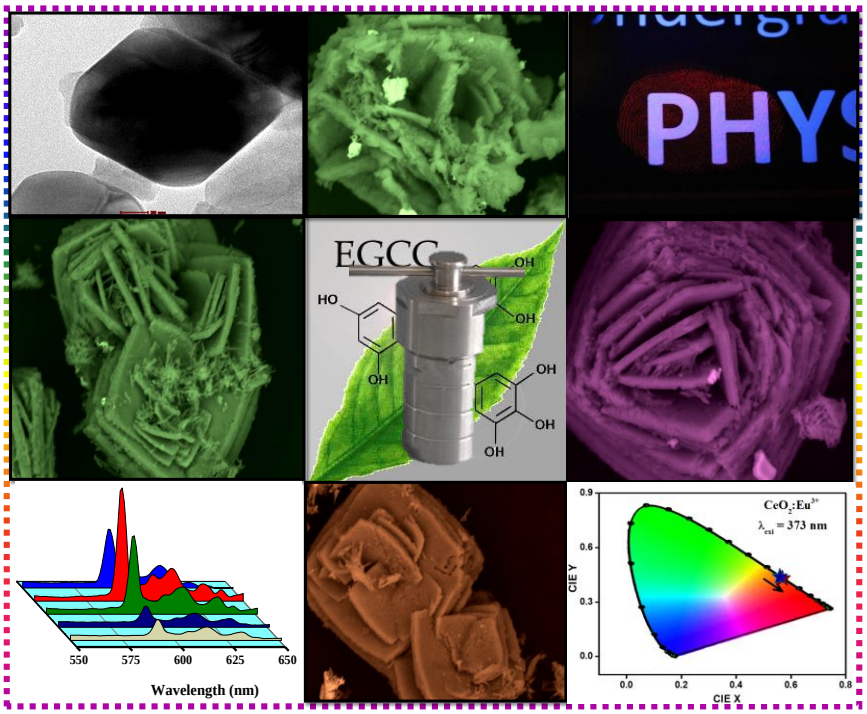

Research highlights

- Hierarchical 3D structures of CeO_2:Eu^{3+} phosphors were prepared by ultrasonication.
- Visualization of LFPs on various surfaces was studied systematically.
- Photometric properties exhibit warm and intense red colour with high purity emission.
- Compounds were useful in optoelectronics, forensic and photocatalysis applications.

Abstract

Novel CeO_2:Eu^{3+} (1-9 mol %) nanophosphors (NPs) with flower-like hierarchical structures and controlled shape and size were effectively synthesized by hydrothermal method using Epigallocatechin gallate (*EGCG*) as bio-surfactant. Optimized NPs was explored as an effective labeling agent for visualization of latent fingerprints (LFPs) on different porous and non-porous surfaces. Visualized fingerprints (FPs) revealed first, second and third-level ridge particulars with high contrast, high selectivity and low background interference. X-ray photoelectron spectral studies (XPS) evident that the presence of oxygen vacancies responsible for the surface modification of these superstructures. The induced oxygen vacancies were also strongly influenced the photoluminescence (PL) properties of the prepared samples. 3D flower-like hierarchical architectures were explored by tuning different experimental parameters. Growth mechanism of 3D architectures developed through two dimensional (2D) flakes involves nucleation, growth, Ostwald ripening and recrystallization. The photometric properties evident that, the prepared samples exhibit intense red color with color purity ~ 80 %. Investigation on visible light photocatalytic degradation of methylene blue (MB) has been examined using these powders. Results discussed were noteworthy for exploring these phosphor materials in multi-functional applications such as optoelectronics, forensic and photocatalysis applications.

Keywords: Hydrothermal synthesis; oxygen vacancy; 3D flower like architectures; latent fingerprints; photocatalysis.

1. Introduction

Fabrication of 3D nano/micro hierarchical morphologies including flowers, spheres, fishbone, octahedron and others with controlled size, shape and surface functionalities offers numerous interests for scientific community because of their outstanding physical and chemical properties [1-3]. From the past few years, fabrication of hierarchical structures by solution based chemical methods significantly recognized due to its capacity to fabricate variety from metals to semiconductors to metal oxide nanocrystals. Since the solution assisted fabrication techniques afford a soft chemical approach where the reactions were carried out at low temperatures (< 250 °C) with the defined control over nucleation and its growth [4, 5]. This offers high purity, homogeneous and large scale fabrication of anisotropic architectural building blocks. In addition, nanoscale dimensional materials can be explored by the efficient and cautious control of thermodynamic parameters and growth kinetics in liquid media by choosing appropriate surfactants or catalyst additives, reaction solvents and ligands [6].

Over past two decades, nanoscience and technology finds wide range of benefits in the area of surface based science due to its nano size and high surface area. This offers new potentials in surface-based science comprising of visualization of LFPs [7, 8]. FPs were considered as major physical evidence for identification of individuals in a crime spot investigation. During investigation, usually impression, patent and LFPs were observed. Amongst, LFPs were the most regular at crime scenes and were invisible to human eye [9]. Therefore, to make them visualize several techniques including, powder dusting, cyanoacrylate fuming, ninhydrin method, 1, 8-Diazafluoren-9-one method, silver nitrate method, and small particle reagent method, were the most extensively used methods due to simple experimental procedure, efficiency and sensitivity. However, many researchers have made several attempts to visualize LFPs which will assist for advanced forensic investigations and to boost the success rate [10]. To overcome from these complications, fluorescent labeling powders were considered to be most efficient and significant agents for

visualize LFPs on both porous and non-porous surfaces owing to their distinctive optical and chemical properties [11, 12]. These labeling powders exhibit several benefits namely smaller crystallite size, exceptional photo- chemical stability, enhanced luminescence property, morphological variations and low toxic nature.

Human safety and standards, environmental problems concern several scientific features were still considered as foremost issues. Dyes from the textile industries were considered as a major organic pollutant in environment because of the presence of highly toxic nature and low resistance to bio-degradation materials [13, 14]. Removal of toxic dyes from waste water, numerous efforts have been made to overcome such ecological issues seems frontward for the clean and healthy environment. Among the many methods, inorganic NPs were new approach for heterogeneous photocatalysis and offer much interest for research fraternity to many air pollutants as well as industrial waste water treatments owing to their high effectiveness, simple and economical benefits [15]. Therefore, many attempts have been made by the researchers to explore novel visible light and UV motivated photocatalysts by utilizing economical and vast solar energy [16, 17].

The rare earth based CeO_2 oxides were attracted much for the past few decades due to their wide spread applications namely solid oxide fuel cells, dye removal treatments, polishing materials, electrode materials for gas sensors, oxygen storage capacity and effective radio protectants for radiation therapy [18-21]. Owing to its remarkable applications, many efforts have been attempted in the fabrication of CeO_2 NPs with hierarchical architectures including nanorods, nanotubes, nanowires, nanoplates, nanobelts and etc., by various chemical and physical routes [22-26]. However, the fabrication of 3D hierarchical CeO_2 structures was rarely accounted. Controlled 3D crystal growth in liquid media phase was much difficult as compared to other methods. This arises due to the fact that the cubic CeO_2

does not exhibit intrinsic driving force for 3D growth this leads to the fabrication of controlled 3D CeO_2 hierarchical structures creates new avenue to researchers.

In the present work, fabrication of controlled 3D flower-like hierarchical $CeO_2:Eu^{3+}$ structures by hydrothermal method using Epigallocatechin gallate (EGCG) as a surfactant was reported. Optimized photometric sample was explored as a labeling agent to visualize the LFPs on various porous and non-porous surfaces. Further, the visible light driven photo degradation properties of $CeO_2:Eu^{3+}$ (3 mol %) NPs on MB dye was extensively investigated.

2. Experimental and Characterization

Fresh tea leaves were collected from tea gardens in the region of Ooty, Tamilnadu, India (11.4064° N, 76.6932° E) and washed several times under running water and then dried in an oven at 60 ^oC. The dried tea leaves were crinkled in an electric blender and then sieved. The extraction was achieved in 250 ml Erlenmeyer flask by mixing 100 ml of 10 % ethanol and 5 gm of dried tea leaves powder. Extraction was done in a water bath at a temperature of 60 ^oC. The extract was separated by filtration and placed in an oven at temperature of 40 ^oC.

The $CeO_2:Eu^{3+}$ (1-9 mol %) NPs were synthesized by hydrothermal route by using EGCG as a surfactant. About 1 mM Cerium (III) nitrate hexahydrate [$Ce(NO_3)_3 \cdot 6H_2O$] and different concentrations of Europium(III) nitrate pentahydrate [$Eu(NO_3)_3 \cdot 5H_2O$] were thoroughly mixed with 20 ml distilled water using magnetic stirrer for ~ 20 min. Subsequently, 5 %W/V of *EGCG* and 15 ml of ethanol was added to form the precursor solution. The resultant solution was transferred to a 100 mL Teflon-lined stainless steel autoclave, sealed and maintained at various temperature (120, 140, 160 and 180 ^oC). The experiment was repeated for various reaction time (2, 4, 6, 8, 10 and 12 h) and concentration of EGCG (5, 10, 20 and 30 %W/V). The final precipitates were separated by centrifugation, washed several times using ethanol and dried in vacuum at 80 °C for 6 h. Fig.1. Shows the

pictorial representation of hydrothermal synthesis of CeO_2:Eu^{3+} (1-9 mol %) NPs using EGCG as a surfactant.

Crystallinity of the prepared samples were estimated using powder X-ray diffractometer (PXRD, Shimadzu 7000) with Cuk_α (1.541 Å) radiation. The morphology of the samples was observed on a Hitachi table top, Model TM 3000 scanning electron microscopy (SEM). Transmission electron microscopy (TEM) was performed on a Hitachi H-8100 accelerating voltage up to 200 KV, LaB_6 filament equipped with EDS (Kevex sigma TM Quasar, USA). The JobinYvon Horiba LABRAM-HR-Visible micro Raman system was used for Raman studies with He-Ne laser (~ 632.8 nm) as the source. The chemical composition was determined by X-ray photoelectron spectroscopy (XPS) using a PHI 5300 with a monochromatic Aluminum source. The UV-Visible absorption/reflectance of the samples was recorded on Perkin Elmer (Lambda-35) spectrometer. For PL studies Jobin Yvon Spectrofluorometer Fluorolog-3 was used with 450W Xenon lamp as an excitation source.

The eccrine LFPs on various surfaces including porous and non-porous surfaces including, glass, aluminium foil, stainless steel, plastic sheet, wooden floor and different color background papers were collected from healthy donor. Before impression, the hands of the donor were thoroughly washed with soap and dried. Afterwards, the fingers were pressed against various surfaces to get LFPs. Then, the optimized CeO_2:Eu^{3+} (3 mol %) NPs was stained on the LFPs by using soft feature brush with smooth brushing method. Finally, developed FPs were visualized under UV 254 nm light by using a Nikon D3100/AF-S Nikkor 50 mm f/2.8G ED lens digital camera. The superiority of enhanced FPs on various porous and non-porous surfaces was evaluated by using Bandey scale developed by UK Home Office [27]. This five point scale system was extensively used to estimate the quality of FPs

only in research circumstance not in legal procedures (Table.1). According to Bandey system, grade 3 or grade 4 FPs were considered for explicit identification of individuals.

In the photocatalytic study, MB dye was used as an organic pollutant in water. The stock solution of MB dye and catalyst (20-180 mgL^{-1}) was prepared using double distilled water. The prepared MB dye and the catalyst solution was added in a circular glass reactor, stirred magnetically to get homogeneous solution and exposed to visible light. The experiment was carried out under ambient condition in between 12 to 2 pm (month of April, Bangalore) with latitude and longitude of 12.60N and 77.31E respectively. By using appropriate setup, the normal light was concentrated onto a reactant solution. Before carrying out the experiments, the reactant solution was kept under dark to obtain balance adsorption and desorption equilibration of the system so that the loss of dye due to adsorption can be taken into account. The experiment was repeated for various concentrations of catalyst and time period. Finally the suspension was centrifuged and analyzed for adsorption of dye before and after visible light illumination.

3. Results and Discussion

The PXRD patterns of pure and CeO_2:Eu^{3+} (1-9 mol %) NPs prepared at ~ 180 ^oC for 12 h with 30 %W/V of *EGCG* was shown in Fig.2 (a). All diffraction profiles were agreeably indexed to cubic fluorite structure of ceria with a JCPDS card No. 81-0792 and space group: Fm–3m (2 2 5) [28]. The sharp and intense diffraction peaks shows high degree of crystallinity of the samples. Further, no impurity peaks were detected, specifying that dopant Eu^{3+} concentration does not influence on phase and purity of the samples. The peak indexed with (111) shifts towards a lower angle side due to crystal lattice expansion after entry of Eu^{3+} ions into the crystal lattice. Further, the effect of Eu^{3+} substitution on the lattice parameter and highest peak positions was shown in Fig.2(c & d). From the figure, it was evident that the lattice parameter as well as the highest peak position varies linearly with the

addition of Eu^{3+} ion concentration. The average crystallite size of the prepared samples was estimated from both Scherrer's relation and W-H plots method as per literature [29] and tabulated in Table 2. The W-H plots of CeO_2:Eu^{3+} (1-9 mol %) NPs was shown in Fig.2 (b). The dislocation density (δ) and stacking fault energy (SFE) was estimated by using following relations;

$$\delta = \frac{1}{D^2} \text{--------(1)}$$

$$\text{SFE} = \left[\frac{2\pi^2}{45\,(3\tan\theta)^{1/2}} \right] \text{--------(2)}$$

A stacking fault was a disorder of the normal stacking sequence of atomic planes in a crystal structure which carries certain stacking-fault energy. The estimated dislocation densities and stacking fault energy were given in Table 2.

Rietveld refinement was used to study the precise structural parameters by using *FULLPROF* software [30]. Fig.3 (a-e) shows the refinement of CeO_2:Eu^{3+} (1-9 mol %) NPs and their corresponding parameters were listed in Table 3. It was evident from the table that, the substitution of Eu^{3+} ions concentration in the host can alter the lattice parameters from 5.4222 to 5.4234 Å. The line mark and subordinate solid line represents the positions of Bragg reflections, observed and estimated intensities difference respectively. Generally, the least squares fitting method was utilized to best fit between observed and estimated intensities. In the present case, we work out Thomson–Cox–Hasting pseudo-Voigt peak profile function for best refinement [31]. The obtained values were well agreed with theoretical values. The quality of refinement values were verified by calculating GOF (goodness of fit) by considering the ratio of R_{wp} and R_{exp}. In the present studies, estimated GOF was found to be 1.06 which confirms authenticated fitting between experimental and

theoretical values. By utilizing refined values, packing diagram was drawn by using diamond software [32] (Fig.3 (f)). In a face centered cubic fluorite type CeO_2 structure, each Ce atoms occupies corner of the cube and synchronized by eight closet-surrounding oxygen (O) atoms, whereas the 4 Ce atoms tetrahedrally co-ordinate with O atoms. And each oxygen ion has four ligancy of Ce cations.

The 3D flower - like hierarchical nanostructures were achieved by altering the reaction time from 2 to 12 h. When the reaction time was 2 and 4 h, 2D randomly oriented sheet like morphology was observed (Fig.4 (a & b)). This may due to crystal splitting that can arises at the partial nuclei surface to form 3D structures. When the reaction time was extended to 6 and 8 h, various 2D sheets undergo self- assembly and to form flower - like structures were observed and depicted in Fig.4 (c & d). Here, flower-like structures were not well - oriented and they were in the primary stage of the growth. When the reaction was prolonged to 10 and 12 h, prominent 3D well oriented flower - like hierarchical nanostructures were observed in Fig.4 (e & f). The pictorial representation of probable growth mechanism of 3D hierarchical flower - like architecture was shown in Fig.4 (A-E).

Fig.5 shows the schematic representation of the morphological modifications from irregular sheet to 3D flower - like hierarchical structures which include nucleation/growth, aggregation, self-assembly and Ostwald ripening was shown in Fig.5. Amongst, Ostwald ripening the self - assembly plays a vital role to form 3D hierarchical nanostructures at the initial stage. After nucleation, particles will grow and start attaching continuously and bond to the other surface in an oriented direction. During Ostwald ripening, tiny and unstable particles serve as sources for growth of large sized flakes with little surface energy.

The effect of EGCG concentration on the morphology of the prepared product was extensively studied. Fig.6 (a-d) shows the SEM images of $CeO_2:Eu^{3+}$ (3 mol %) NPs prepared with different concentrations (5, 10, 20 and 30 %W/V) of EGCG extract with fixed

temperature and sonication time at ~ 180 ^{o}C and 12 h respectively. When the concentration of EGCG was ~ 5 and 10 %W/V, the disorderly arranged flake - like structures was observed (Fig.6 (a & b)). As the concentration of EGCG was increased to 20 - 30 %W/V, the growth inhibits in one particular direction and it leads to oriented growth of flakes to form flower-like morphology (Fig.6 (c & d)). The pictorial representation of the proposed growth mechanism for the 3D flower-like hierarchical structures in the presence of a surfactant was shown in Fig.7.

In the present work, we established that the reaction temperature plays a key role for flower - like architect of prepared product while optimized reaction parameters such as time and concentration of EGCG (12 h and 30 %W/V) were kept fixed. At 120 ^{o}C, randomly oriented rough surfaced flakes were obtained (Fig.8 (a)). When the reaction temperature was increased to 140 ^{o}C and 160 ^{o}C, self-assembled 3D flower like architectures were observed (Fig.8 (b & c)). Further, when the temperature was increased to 180 ^{o}C, flower - like structures with dense and thin petals was achieved (Fig.8 (d)).

Fig.9 shows the TEM, HRTEM image and SAED patterns of the CeO_2:Eu^{3+} (3 mol %) NPs. As can be seen from the figure that the crystallites were almost flake - like morphology with size ~ 20 nm, which was in good agreement with PXRD results (Fig.9 (a)). The HRTEM image shows that the product was highly crystalline in nature (Fig.9 (b)) with the interplanar spacing (d) values ranges in between 0.28 - 0.30 nm (Fig. 9 (d)). SAED pattern confirms that, all the diffraction rings were well indexed with hkl plane numbers (Fig.9 (c)).

Fig.10 (a & b) shows the Raman spectra of pure and Eu^{3+} (1-9 mol %) doped CeO_2 NPs and its enlarged portion. The spectra exhibit four characteristic modes at ~ 254, 460, 546 and 612 cm^{-1} [33]. The mode at ~ 254 and 460 cm^{-1} were attributed to twice degenerated 2TA and first order F2g respectively. An F_{2g} mode confirms the fluorite cubic structure of the

prepared samples and also signifies symmetrical stretching vibration of the CeO_8 vibrational unit. A broad and asymmetric mode ~ 460 cm^{-1} was red shifted as compared to pure sample owing to oxygen defects, phonon confinement, size distribution, deviation in phonon relaxation and strain present in the sample [34, 35]. The other modes at ~ 546 and 612 cm^{-1} were due to oxygen vacancies (intrinsic and extrinsic) defect. The relative intensities of Raman modes of at ~ 460, 546 and 612 cm^{-1} can be calculated from the relation [36]:

$$\frac{Oxygen\ vacancies}{F_{2g}} = \frac{\left(Area_{R_{Ce-O}} + Area_{R_{dopant}}\right)}{Area\ F_{2g}} \text{ ---------- (3)}$$

The rate of oxygen vacancies were estimated and given in Table 4. It was observed that, initially the rate of oxygen vacancies were more for pure sample as compared to doped CeO_2 NPs. Finally, the value diminished and reached an approximate balance with further increase in the Eu^{3+} dopant concentration. The variation in the value can be mainly attributed to the amount of the dopant. At the beginning, Eu^{3+} was introduced into bulk CeO_2, and more extrinsic oxygen vacancies were achieved except intrinsic oxygen vacancies. Consequently, the rate of oxygen vacancies rapidly increased. When an excessive amount of the dopants was added, the oxygen vacancy concentration increased and eventually reached a steady plateau level in order to maintain electron neutrality of the system. The mode at ~ 612 and 546 cm^{-1} were due to intrinsic and extrinsic oxygen vacancies respectively. The probable reaction for intrinsic oxygen vacancies [37] were followed as;

$$Ce_{Ce} + 2O_o \rightarrow V'''' + 2V_o^{\bullet\bullet} + CeO_2 \text{ ---------- (4)}$$

$$Ce_{Ce} \rightarrow V_{Ce}'''' + Ce_i^{\bullet\bullet\bullet\bullet} \text{ ---------- (5)}$$

$$O_o \rightarrow V_o^{\bullet\bullet} + O_i'' \text{ ---------- (6)}$$

Besides, the average crystallite size of the CeO_2:Eu^{3+} NPs scale down to nano range, leads to more oxygen loss. The extrinsic oxygen vacancies were initiated owing to substitution of

Eu^{3+} ions into host Ce^{4+} site results in oxygen ions loss. The plausible reaction mechanism for extrinsic oxygen vacancies [38] was given by following reactions:

$$(1-x)CeO_2 + {}^{x}\!/_{2}\, Eu_2O_3 \rightarrow (1-x)\, Ce_{Ce} + xEu'_{Ce} + (2-{}^{x}\!/_{2})\, O_o + (2-{}^{x}\!/_{2})\, O_o + {}^{x}\!/_{2}\, V_o^{\bullet\bullet} \quad \text{----------} \quad (7)$$

where, Eu'_{Ce}; occupancy of Eu ions in a Ce^{4+} site, $V_o^{\bullet\bullet}$; O^{2-} vacancy, Ce_{Ce}; remaining Ce^{4+} ions in the CeO_2 host and O_o; oxygen present in the host lattice. The classification of the defects was estimated by using Raman spectra. The ~ 546 cm^{-1} vibration mode was due to association of extrinsic oxygen vacancies with dopant Eu^{3+} ions and was given by following reaction:

$$(Eu'_{Ce} - V_o^{\bullet\bullet})^{\bullet} \text{ and } (2Eu'_{Ce} - V_o^{\bullet\bullet})^{x} \text{ ----------} (8)$$

The intensity at ~ 546 cm^{-1} vibrational mode does not exhibit any major variation, shows that incomplete dissociation of oxygen vacancies from defect cluster. It evident that, for higher dopant Eu^{3+} concentration would form composite arrangement of defects and entrap oxygen vacancies and hence mobile ions. In the other hand, mode at ~ 612 cm^{-1} was attributed to defect spaces which arises because of connection of intrinsic oxygen vacancies with reduced host cations. The variation of intensity at ~ 612 cm^{-1} mode can be revealed in terms of dissociation of oxygen vacancies from extrinsic vacancies cluster.

Further, XPS analysis was performed in order to reveal the chemical composition and valence state of the chemicals in the synthesized samples. Fig.11 (a) shows the wide survey scan XP spectrum of CeO_2:Eu^{3+} (3 mol %) NPs. The spectrum exhibits peaks C 1s, O 1s, Ce 3d and Eu 3d at ~ 283, 526, 911 and 1165 eV respectively [39]. Among the carbon peak C 1s at ~ 283 eV was due to carbon dioxide contamination on the surfaces and also it was considered as a reference binding energy (Fig.11 (b)). The deconvolution spectrum of O 1s peak shows peaks at binding energy ~ 528, 531 and 532.4 eV which attributed to lattice

oxygen ions, absorbed oxygen and lattice oxygen ions in CeO_3:Eu^{3+} NPs respectively (Fig.11 (c)). The Ce 3d3/2, 5/2 spectra of CeO_2:Eu^{3+} (3 mol %) NPs recorded between ~ 875 and 925 eV was shown in Fig.11 (d). The spectrum enclosed v and u multiplets were attributed to the spin–orbit split $^3d_{5/2}$ and $^3d_{3/2}$ core holes. Each multiplet consists of several components and the highest binding energy components ν''' and u''' (at ~ 897 and 915 eV) were due to $3d^9 4f^0 O\ 2p^6$ final state. The lowest energy components ν', ν'', u' and u'' (at ~ 882, 885, 901 and 905 eV) were attributed to $3d^9 4f^2$ O $2p^4$ and Ce $3d^9 4f^1$ O $2p^5$ final state. The peaks at ~ 1164 and 1134 eV were related to the binding energy of Eu^{3+} $^3d_{3/2}$ and Eu^{3+} $^3d_{5/2}$, which specified that Eu ions in the CeO_2 lattices occurred in the trivalent form (Eu^{3+}). These results suggest that the CeO_2:Eu^{3+} NPs possess europium ions in the trivalent (3+) form, with small portion of Ce^{3+} ions [40-42].

The electronic band structure of CeO_2 results due to the full Oxygen 2p orbital and empty Cerium 5d orbital forms the valence band and conduction band respectively. Cerium 4f orbital lies between these two orbital and above the Fermi level. In defect free material, Cerium 4f orbital was completely empty because all Ce were in +4 states**.** The Diffuse reflectance (DR) spectra for pure and the CeO_2:Eu^{3+} (1-9 mol %) NPs was recorded in wavelength range ~ 200-1100 nm was shown in Fig.12 (a). The Kubelka-Munk (KM) function was utilized to estimate the energy band gap of the prepared samples [43]. The plot of $F(R)^2$ v/s energy (hv) was plotted, as shown in Fig.12 (b). Band edge of pure and CeO_2:Eu^{3+} (1-9 mol %) NPs were estimated by extrapolating the curve $F(R)^2$ to zero [44]. The band edges measured by extrapolation and were listed in Table 2. Generally the deviation in the band edge or gap was related to certain factors i.e. variation in crystallite size, lattice parameter, oxygen vacancies etc. As can be seen from the table that, the lattice parameter 'a' was found to decrease in Eu^{3+} doped samples. Further, it was witnessed from PXRD studies that undoped sample has higher concentration of oxygen vacancies as well as

lattice parameter was found to be higher due to formation of Ce^{3+} ions. This higher value of lattice parameter leads as a result of the shift in the band edge towards higher values.

Another mechanism which was associated to the observation of blue shift in band gap with decrease in particle size was due to quantum confinement effect [45]. This can be observed only if the nanoparticles size becomes comparable with the Bohr radius of the respective material. The Bohr radius for cerium oxide was ~ 9 nm [46]. Singh *et. al* has reported quantum confinement effect in CeO_2 NP with particle size variation lying in the range ~ 3 - 5 nm [45]. In the present work, the average crystallite size of the prepared CeO_2:Eu^{3+} (1 mol %) NPs was ~ 8.8 nm and lies well within the range where quantum confinement effects were expected. Sunekawa *et. al*. described the blue shift in CeO_2 NP arises due to the charge transfer transition and was not due to the quantum size effect [46]. In their detailed study, they varied the particle size and smaller sized particle, the valence of Ce ions was found to be lower than +4. Hence, the extracted gap between the 2p (O) and 4f (Ce) states was found to increase with decreasing particle size with corresponding increase in Ce^{3+} concentration. So it can be concluded that the blue shift in the band gap of as-prepared sample can be due to the higher concentration of Ce^{3+} which was connected with higher concentration of oxygen vacancies and hence lattice expansion [47, 48].

The excitation spectrum of CeO_2:Eu^{3+} (3 mol %) NPs under λ_{emi}= 611 nm, as shown in inset of Fig.13 (a). The spectra exhibits intense peaks at ~ 376, 417 and 447 nm were attributed to $^7F_0 \rightarrow {}^5L_7$, $^7F_0 \rightarrow {}^5D_3$, and $^7F_0 \rightarrow {}^5D_2$ transitions of Eu^{3+} ions in the CeO_2 host respectively. Fig.13 (a) shows the PL emission spectra of CeO_2:Eu^{3+} (1-9 mol %) NPs excited at 373 nm wavelength at room temperature (RT). The spectra displays a peak at ~ 592, 611 and 630 nm were attributed to $^5D_0 \rightarrow {}^7F_1$, $^5D_0 \rightarrow {}^7F_2$ and $^5D_0 \rightarrow {}^7F_3$ $4f^6$ configuration of Eu^{3+} ions, respectively [49]. However, the samples were excited at ~ 447 nm exhibits peaks at ~ 612, 738 nm and broad peak at ~ 630-704 nm were attributed to $^5D_0 \rightarrow {}^7F_0$, $^5D_0 \rightarrow {}^7F_4$ and $^5D_0 \rightarrow {}^7F_2$

transitions, as shown in Fig.13 (b). Generally, various experimental parameters were more influenced on optical properties. The PL emission spectra of CeO_2:Eu^{3+} (3 mol %) NP synthesized at various temperature (120, 140, 160 and 180 ˚C) under 393 nm excitation wavelength, as shown in Fig13 (c). It can be observed from the figure that, when reaction temperature increases, PL intensity of the sample increases. At lower temperature, samples may contains optical quenching centers, which may degrade the emission intensity gradually. These quenchers get reduced significantly on increase of reaction temperature. Fig13 (d) shows the PL emission spectra of CeO_2:Eu^{3+} (3 mol %) NP synthesized with various reaction time (~ 2, 4, 6, 8, 10 & 12 h) under λ_{Exci} = 393 nm at RT. The spectra exhibit similar trend, however, overall emission intensity was observed to be enhanced in sample prepared with 12 h reaction time due to increase in crystallinity of the prepared sample. The weak emission peak at 611 nm was due electric –dipole (ED) transition $^5D_0 \rightarrow {}^7F_2$ which was hypersensitive in the host matrix. The intense emission peak at ~ 592 nm was assigned to $^5D_0 \rightarrow {}^7F_1$ transition and ascribed to magnetic dipole (MD) transition which was insensitive to site symmetry. Asymmetry ratio (A_{21}) between ~ 611 nm ($^5D_0 \rightarrow {}^7F_2$) and ~ 592 nm ($^5D_0 \rightarrow {}^7F_1$) was used to determine the host structures and was calculated by following equation [50];

$$A_{21} = \frac{\int I_2(^5D_0 \rightarrow {}^7F_2)d\lambda}{\int I_1(^5D_0 \rightarrow {}^7F_1)d\lambda} \text{ --------- (9)}$$

where, I_1 and I_2; intensity at 611 nm and 592 nm respectively. Generally, the higher value of A_{21} explains the occupancy of Eu^{3+} ions in a host site with a low symmetry and without an inversion center. The plot of A_{21} v/s dopant Eu^{3+} ions concentration was shown in Fig.13 (e). It was clearly apparent that, the value of A_{21} decreases upto 3 mol % and thereafter it increases linearly as concentration of Eu^{3+} ions increases. This evident that the substitution of dopant Eu^{3+} ions in a CeO_2 host would changes the host structure. The dopant Eu^{3+} ions positioned with inversion site symmetry when the lower concentration of Eu^{3+} ions, while at

higher concentrations, majority of dopant ions reside in without inversion site symmetry. The host CeO_2 was a face centered cubic fluorite type structure with an Fm-3m space group. In a typical structure, Ce atoms occupies corner of the cube and synchronized by eight closet-surrounding oxygen (O) atoms, whereas the 4 Ce atoms tetrahedrally co-ordinate with O atoms. The effect of dopant Eu^{3+} on CeO_2 unit cell was shown in Fig.14. In the prepared samples, dopant Eu^{3+} ions were replaces the Ce^{4+} ions at the corners of the unit cell. Due to different cationic charge, oxygen vacancies were created to stabilize the charge dissimilarity. Usually, oxygen vacancies choose adjacent neighbor (AN) or next adjacent neighbor (NAN) sites of the dopant ions. As per literature survey, dopants having higher ionic radii as compared to Ce^{4+} ion would drive oxygen vacancies to NAN site and hence RE ions retain Oh symmetry of cubic Ce^{4+} sites. At lower concentrations of Eu^{3+} ions, creation of oxygen vacancies were less and symmetry of a host was not much influenced. While at higher concentration, number of oxygen vacancies was higher and leads to creation of new surrounding in the CeO_2 host. The new nearby environment perturbs the symmetry of the host. With further increase of Eu^{3+} ions concentration, any Eu^{3+} ions resides in the host sites with a low symmetry and without an inversion center, which alters the emission spectra. The effect of dopant Eu^{3+} ions on emission intensity at ~ 592 nm under 373 nm excitation wavelengths was shown in Fig.13 (e). It reveals that, the PL emission intensity increases up to 3 mol % of Eu^{3+} and afterwards diminishes linearly due to self-concentration quenching which attributed to transfer of energy among dopant Eu^{3+} ions in host material. Determination of interaction mechanism between dopants which usually arises due to exchange interaction, radiation re-absorption or a multiple –multiple interaction was a probe to self-concentration quenching nature. In view of this, it was essential to estimate the critical distance (R_c) between two adjacent Eu^{3+} ions as suggested by Blasse and was given by following relation [51];

$$R_c = 2\left(3V/4\pi N X_c\right)^{1/3} \text{ ---------- (10)}$$

where, V; unit cell volume, X_c; critical concentration of Eu^{3+} ions and N; number of crystallographic sites per unit cell. In the present case, calculated value of R_c was found to be ~ 10.23 Å. According to literature, the value of R_c between neighbor dopant ions was less than 5 Å which leads to exchange interaction. But in the present case, the estimated value of R_c was greater than the 5 Å which indicates that exchange interaction was not responsible for energy transfer between Eu^{3+} ions. The overlapping of PL excitation and emission spectra of dopant and host was not observed which validate non-existence of radiation re-absorption. Therefore, the multiple –multiple interaction was mainly liable for non-radiative energy transfer between adjacent Eu^{3+} ions. According to Van Uitert's theory, the type electric multipolar interaction was estimated by using the following relation [52];

$$\frac{I}{\chi} = K\left[1+\beta(\chi)^{\frac{Q}{3}}\right]^{-1} \text{ ---------- (11)}$$

where, χ ; concentration of Eu^{3+} ions, Q ; a constant having values 3, 6, 8 and 10 indicates electric multipolar interaction, dipole – dipole (d - d), dipole – quadrupole (d - q) and quadrupole – quadrupole (q - q) interactions and K & β ; constants. The value of Q was estimated by logarithmic plot of (I/χ) v/s (χ) and was depicts in Fig.13 (f). The figure clearly confirms that the plot was approximately linear and the value of slope was found to be ~ -0.980. The obtained value of Q was found to be 7.66 and was almost equal to theoretical value 8 for the q - q interaction. This indicates that q-q interaction was main interaction mechanism which responsible for the concentration quenching in CeO_2:Eu^{3+} (1-9 mol %) NP.

Fig.15 (a) shows the Commission Internationale de L'Eclairage (CIE) diagram for CeO_2:Eu^{3+} (1-9 mol %) NPs excited at 373 nm. Generally, the emission color of samples can be characterized by the chromaticity co-ordinates (x, y) [53, 54]. The CIE co-ordinates of CeO_2:Eu^{3+} (1- 9 mol %) NPs were estimated using PL emission spectra and listed in Table.4.

It was observed from figure that, the CIE co-ordinates of CeO_2: Eu^{3+} (1-9 mol %) NPs were located in the intense red region and tuning towards National Television System Committee (NTSC) standard values of pure red color (0.67, 0.33) region. The correlated color temperature (CCT) of CeO_2: Eu^{3+} (1-9 mol %) NPs were calculated according to literature [55] and summarized in Table 5. The CCT diagram of CeO_2: Eu^{3+} (1-9 mol %) NPs was shown in Fig.15 (b). The color purity of prepared NPs was also analyzed using the relation [56];

$$color\ \ purity = \frac{\sqrt{(x_s - x_i)^2 + (y_s - y_i)^2}}{\sqrt{(x_d - x_i)^2 + (y_d - y_i)}^2} \times 100\% \quad \text{---------- (12)}$$

where, (x_s , y_s),(x_d , y_d) and (x_i , y_i) ; the co-ordinates of a sample point, dominant wavelength and illuminant point respectively. The color purity of the synthesized samples were estimated and listed in Table 5. The above results indicate that the present phosphor may be quite useful for warm LED's applications. Further, the quantum efficiency (QE) of the prepared products was calculated by the following relation;

$$QE = \frac{Number\ of\ \ photons\ \ \ emitted}{Number\ of\ \ photons\ \ \ absorbed} = \frac{E_c - E_a}{L_a - L_c} \quad \text{---------- (13)}$$

where, E_c ; the integrated luminescence of the phosphor caused by direct excitation, E_a ; the integrated luminescence from the empty integrating sphere (blank, without sample), L_a; the integrated excitation profile from the empty integrating sphere, L_c; the integrated excitation profile when the sample was directly excited by the incident beam. In the present case, the QE of the samples were estimated and tabulated in Table 5.

In addition, the optimized CeO_2: Eu^{3+} (3 mol %) NPs was utilized for visualization of LFPs on glass was shown Fig.16 (a-e). From the figure, it was evident that the synthesized product was noticeably visualized level 1 and 2 minutiae ridges such as bifurcation, whorl,

loop, island and lake were effortlessly due to their smaller crystalline size. The level 3 patterns (sweat pores) were innovative details for authentication of individuals in forensic analysis where partial FPs or lack of explicit level 2 details. From the figure, it was evident that in addition to level 2 patterns, level 3 substructures (sweat pores) from which the sweat was secreted, could also be enhanced (Fig.16 (d)). Further, the LFPs were visualized by CeO_2: Eu^{3+} (3 mol %) NP on glass plate exposed under UV 254 nm and 365 nm illuminations (Fig. 16 (f & g)). The obtained results indicate that the optimized NPs reveal the whole FPs with better contrast and sensitivity under 254 nm.

However, a series of experiments were performed to visualize the LFPs on various non-porous surfaces such as aluminum foil, stainless steel, plastic sheet, wooden floor sheet and compact disk cover were performed were shown in Fig.17. A well-defined sharp and level 2 minutiae ridge substructure patterns were noticeably visualized on all surfaces with any background hindrance (Fig.17 (b, d, f, h & j)). In addition, the comparison of quality of FPs visualized by using CeO_2: Eu^{3+} (3 mol %) NPs under visible light (Fig.17 (a, c, e, g & i)) and UV 254 nm were graded according to Bandey's scaling scheme (Table.1). It was evident that, the almost grade 4 images were visualized by using prepared optimized sample. This shows that, the present fabricated method was multi -purpose which can be visualizing LFPs on non-porous surfaces.

Generally, the visualization of LFPs on porous surfaces was practically challenged for forensic investigators due to absorption of the constituents of LFPs by these materials. To evaluate the versatility of the prepared sample, LFPs were visualized on different porous surfaces namely magazine covers and Indian currency with dissimilar background colors under visible and UV 254 nm light (Fig.18 & 19). Interestingly, high contrast, sufficient quality clearer ridge patterns on all surfaces were evidently determined without any background interference.

In the present work, it was explored the use of CeO_2: Eu^{3+} (3 mol %) NPs as labeling agents for the effective visualization of LFPs on various porous and non-porous surfaces. From the images, it can be evident that grade 4 images (according to Bandey's grading scale), would permit explicit determination of an individuals. The visualized LFPs exhibit high efficiency (because procedure involves simple setup and rapid and performed less than 5 min) and high sensitivity (because no color hindrance and chemical constituents can be observed due to smaller crystalline size).

The photocatalytic degradation of MB dye under visible light irradiation in the presence of fabricated CeO_2:Eu^{3+} (3 mol %) NP was investigated and the effect of concentration of catalyst on photo degradation was systematically analyzed. The typical MB dye has vast applications ranging from textile to paper industry. The heteropolyaromatic MB dye containing heteroaromatic, cationic thiazine ($C_{16}H_{18}ClN_3S$: tetra methylthionine chloride) and was readily soluble in water results to blue solution [57].

The photodegradation of MB with different concentration of CeO_2:Eu^{3+} (3 mol %) NP (20 mgL^{-1} to 180 mgL^{-1}) obtained at 12 h with 30 % W/V of EGCG under visible light was shown in Fig.20 (a). From the figure, it was evident that the percentage degradation of MB dye was found to be ~ 6 %, 12 %, 34 %, 61 % and 93 % for 20, 60, 100, 150 and 180 mgL^{-1} respectively (Inset of Fig.20 (a)). The enhanced visible light driven MB dye degradation % by catalyst concentration was due to (i) high photon absorption rate, (ii) improved photoactive sites by light reflection and scattering, (iii) better active sites on the surface which can provide supportive contact between dye and catalyst and (iv) enhanced surface chemical energy of catalyst and improved electron-cavity formation. In addition, various parameters such as size, morphology and electronic structure properties of catalytic material can also affect the photocatalytic property. In our present case, we could observe 3D hierarchical architectures in the SEM results. Therefore, the enhanced photocatalytic

degradation was predicted to morphology and electronic structural aspects. Above factors enhances the photo driven charge carriers on the surface of catalytic material results increase in the number of oxidizing agent and leads to improved visible light driven photocatalytic activity.

Further, a set of experiments were performed to know the effect of photocatalyst CeO_2:Eu^{3+} (3 mol %) NP on MB dyes degradation under visible light. The catalyst 180 mgL^{-1} of CeO_2:Eu^{3+} (3 mol %) NP and MB dye solutions were stirred vigorously to get uniform solution and the absorption spectra were recorded under light – off and visible light on conditions with different time period was shown in Fig.20 (b). The spectra displays a maximum absorption at a time of ~ 180 min and corresponding % degradation was found to ~ 95 %. The percentage of degradation also decreases gradually as degradation time decreases and was shown in inset Fig. 20 (b). This enhanced photocatalytic degradation was mainly due to electronic structural properties of the prepared CeO_2:Eu^{3+} (3 mol %) NP. As the dopant (Eu^{3+}) substituted in CeO_2 host lattice may alter the electron density of the material by changing cationic valence state and concentration of oxygen. The large number of electron – holes pairs were required to begin oxidation – reduction reactions for photo degradation of MB dye. In the present work, the Eu^{3+} doped CeO_2 samples exhibits decreased energy band gap as compared to pure CeO_2, therefore, reduced band gap provides necessary e^- – h^+ pairs for oxidation – reduction reactions.

However, the time dependent absorbance spectra of the CeO_2:Eu^{3+} (3 mol %) NP with flake and flower - like structures as catalysts on MB dye under visible light irradiation were studied, as shown in Fig.20 (c & d). The maximum absorption peaks for flake and flower - like structures was found to be ~ 0.62 and 0.66 respectively and decreases gradually with increasing visible light irradiation time. When visible light irradiation was at 180 min, the absorption peak dropped drastically for a sample with flower like morphology compared to

flake structure. The intense blue color of the starting MB solution faded as the irradiation time increased. The color change of the MB solution indicates that MB was degraded. The efficiency and rate constant of photodegradation of MB dye was calculated using absorption maximum and the degradation value. The efficiency of de-colorization of CeO_2:Eu^{3+} (3 mol %) NP flake and flower like structure samples were calculated and found to be ~ 76.81 % and 90 % respectively. The apparent rate constant of photocatalytic degradation of MB was determined from the plot between At/A_0 and irradiation time, as shown in Fig. 20 (e). The apparent rate constant was found to be ~ 0.5795 for flakes and ~ 0.8419 for flower like structures respectively. These results evident that, the flowers like structure show excellent visible light photocatalytic performance on MB degradation than flak like structure. It has been reported that, the higher crystallization can usually lead to enhanced photocatalytic activity, by suppressing the recombination of photogenerated holes and electrons. Oxide materials, which possess a larger lattice distortion, have higher photocatalytic activities, by virtue of increasing the additional routes of trapping holes and decreasing the recombination rate of electron–hole pairs [58].

The e^- – h^+ pairs offers efficient path for oxidation and reduction reactions to degradation of MB dye. The generated electrons react with molecular oxygen and produce hydrogen-peroxide molecules in the aqueous medium and expressed by the following reactions;

$$(h\nu > E_g) + catalyst \rightarrow e^-_{CB} + h^+_{VB} \text{ ---------- (13)}$$

$$ne^-_{CB} + nO_2 \rightarrow n\left(O_2^-\right) \text{ ---------- (14)}$$

$$n e^-_{CB} + nO_2 + nH_2O \rightarrow H_2O_2 \text{ ---------- (15)}$$

Conversely, the generated holes produce hydroxyl radicals from the water. These hydroxyl radicals act as an influential oxidizing agent to degradation of pollutant MB and expressed by the following reactions;

$$H_2O + (h^+) \rightarrow {}^*OH + H^+ \text{ ---------- (16)}$$

$$MB + {}^*OH \rightarrow CO_2 + H_2O \text{ ---------- (17)}$$

$$MB + O_2^- \rightarrow CO_2 + H_2O \text{ ---------- (18)}$$

$$\bar{e}_{CB} + h^+_{VB} \rightarrow h\nu + recombination - - - - - - - - - - (19)$$

Therefore, the energetic adsorption and redox reactions of CeO_2:Eu^{3+} (3 mol %) NP were responsible for high catalyst performance under visible light.

The PL studies of CeO_2:Eu^{3+} (3 mol %) NPs exhibits excellent emission properties due to enhanced electronic transitions. In addition, average crystallite size estimated from PXRD inferred that the CeO_2:Eu^{3+} (3 mol %) NPs exhibits smaller size as compared to pure CeO_2. The small sized CeO_2:Eu^{3+} (3 mol %) NPs has larger surface area and exhibits higher adsorption reactions of MB dye on the surface and also enhanced transfer rate of charge carriers towards the surfaces of small sized NPs. The schematic diagram of photocatalytic activity of optimized CeO_2:Eu^{3+} (3 mol %) NPs on MB dyes under visible light irradiation was shown in Fig.21.

4. Conclusions

Large scale controlled 3D CeO_2: Eu^{3+} (1-9 mol %) hierarchical flowers like structures were fabricated by a simple bio-inspired facile hydrothermal route using EGCG as surfactant. PXRD results confirm the cubic phase of the prepared product. Further a suitable reaction time, temperature and surfactant afford adequate energy input to endorse the reaction speed

and strong attractive interactions resulted controlled nucleation and growth of crystals were studied. PL emission spectra displays peaks at ~ 592, 611 and 630 nm were attributed to $^5D_0 \rightarrow {}^7F_1$, $^5D_0 \rightarrow {}^7F_2$ and $^5D_0 \rightarrow {}^7F_3$ $4f^6$ configurations of Eu^{3+} ions, respectively. At lower concentrations of Eu^{3+} ions, creation of oxygen vacancies were less and symmetry of a host was not much influenced. While at higher concentration, the number of oxygen vacancies was higher and lead to the creation of new surrounding in the CeO_2 host. Additionally, the photometric properties evident that the prepared CeO_2: Eu^{3+} (3 mol %) NPs could serve as an alternative material to the expensive nitride red phosphor. Optimized composition of the product has been utilized as labeling agent for visualization of LFPs on various porous and non-porous surfaces. Visualized fingerprints exhibited Bandey system grade 3 or grade 4 fingerprints and were considered for explicit identification of individuals. Photocatalytic investigations revealed that the visible light induced photocatalytic activity enhanced the degradation of MB dye.

Acknowledgement

The author Dr. H Nagabhushana thanks VGST, Govt. of Karnataka, India [VGST/KFIST-4/GRD-489] for the sanction of this Project.

References

[1] V. Polshettiwar, B. Baruwati and R. S. Varma, Self-assembly of metal oxides into three-dimensional nanostructures: synthesis and application in catalysis, ACS Nano, 3 (2009) 728–736.

[2] L. Zhang, W. Niu, G. Xu, Synthesis and applications of noble metal nanocrystals with high-energy facets, Nano Today, 7 (2012) 586–605.

[3] J. Guan, L. Liu, L. Xu, Z. Sun, Y. Zhang, Nickel flower-like nanostructures composed of nanoplates: one-pot synthesis, stepwise growth mechanism and enhanced ferromagnetic properties, Cryst Eng. Comm.13 (2011) 2636–2643.

[4] T. Nguyen, C. Dinh, T. Do, A general procedure to synthesize highly crystalline metal oxide and mixed oxide nanocrystals in aqueous medium and photocatalytic activity of metal/oxide nanohybrids, Nanoscale, 3 (2011) 1861–1873.

[5] K. Namratha and K. Byrappa, Novel solution routes of synthesis of metal oxide and hybrid metal oxide nanocrystals, Prog. Cryst. Growth Ch. 58 (2012)14–42.

[6] C. N. R. Rao, H. S. S. R. Matte, R. Voggu, A. Govindaraj, Recent progress in the synthesis of inorganic nanoparticles, Dalton T. 41 (2012) 5089–5120.

[7] G.P. Darshan, H.B. Premkumar, H. Nagabhushana, S.C. Sharma, B. Daruka Prasad, S.C. Prashantha, Neodymium doped yttrium aluminate synthesis and optical properties – A blue light emitting nanophosphor and its use in advanced forensic analysis, Dyes Pigments. 134 (2016) 227-233.

[8] H. J. Amith Yadav, B. Eraiah, H. Nagabhushana, G. P. Darshan, B. Daruka Prasad, S. C. Sharma, H. B. Premkumar, K. S. Anantharaju, G. R. Vijayakumar, Facile ultrasound route to prepare micro/nano superstructures for multifunctional applications, ACS Sustain Chem Eng., 5 (2017) 2061–2074.

[9] M. Dhanalakshmi, H. Nagabhushana, G.P. Darshan, R.B. Basavaraj, B. Daruka Prasad, Sonochemically assisted hollow/solid $BaTiO_3:Dy^{3+}$ microspheres and their applications in effective detection of latent fingerprints and lips prints, J. Sci.: Adv. Mater. Devices. http://dx.doi.org/10.1016/j.jsamd.2017.02.004.

[10] G.P. Darshan, H.B. Premkumar, H. Nagabhushana, S.C. Sharma, S.C. Prashantha, B. Daruka Prasad, Effective fingerprint recognition technique using doped yttrium aluminate nano phosphor material, J. Colloid Inter. Sci. 464 (2016) 206-218.

[11] R.B Basavaraj, H. Nagabhushana, G.P. Darshan, B. Daruka Prasad, S. C. Sharma, K.N. Venkatachalaiah, Ultrasound assisted rare earth doped Wollastonite

nanopowders: Labeling agent for imaging eccrine latent fingerprints and cheiloscopy applications, J. Ind. Eng. Chem. 51 (2017) 90-105.

[12] M. Saif, MagdyShebl, A.I. Nabeel, R. Shokry, H. Hafez, A. Mbarek, K. Damak, R. Maalej, M.S.A. Abdel-Mottaleb, Novel non-toxic and red luminescent sensor based on Eu^{3+}:$Y_2Ti_2O_7/SiO_2$ nano-powder for latent fingerprint detection, Sensor Actuat B-Chem., 220 (2015) 162-170.

[13] T.S. Natarajan, M. Thomas, K. Natarajan, H.C. Bajaj, R.J. Tayade, Study on UV-LED/TiO_2 process for degradation of Rhodamine B dye, Chem. Eng. J.169 (2011) 126–134.

[14] A. Chithambararaj, N. S. Sanjini, A. C. Bose, S. Velmathi, Flower-like hierarchical h-MoO_3: new findings of efficient visible light driven nano photocatalyst for methylene blue degradation, Catal. Sci. Technol., 3 (2013) 1405–1414.

[15] M.H. Ehrampoush, G.R. Moussavi, M.T. Ghanian, S. Rahimi, M. Ahmadian, Removal of methylene blue dye from textile simulated sample using tubular reactor and TiO_2/UV-C photocatalytic process, Iran. J. Environ. Healt. 8 (2011) 35–40.

[16] F.E. Oropeza, B. Davies, R.G. Palgrave, R.G. Egdell, Electronic basis of visible region activity in high area Sn-doped rutile TiO_2 photocatalysts, Phys. Chem. Chem. Phys.13 (2011) 7882–7891.

[17] D. Mariotti, H. Lindstrom, A. Chandra Bose, K. Ostrikov, Monoclinic β-MoO_3 nanosheets produced by atmospheric microplasma: application to lithium-ion batteries, Nanotechnology, 19 (2008) 495302.

[18] N.S. Arul, D. Mangalaraj, P.C. Chen, N. Ponpandian, C. Viswanathan, Self- assembly of Co doped CeO_2 microspheres from nanocubes by hydrothermal method and their photodegradation activity on AO7, Mater. Lett. 65 (2011) 3320–3322.

[19] R.C. Deusa, C.R. Foschinic, B. Spitovad, F. Mourab, E. Longoc, A.Z. Simoes, Effect of soaking time on the photoluminescence properties of cerium oxide nanoparticles, Ceram. Int. 40 (2014) 1–9.

[20] J. Zhang, H. Kumagai, K. Yamamura, S. Ohara, S. Takami, A. Morikawa, H. Shinjoh, K. Kaneko, T. Adschiri, A. Suda, Extra-low-temperature oxygen storage capacity of CeO_2 nanocrystals with cubic facets, Nano Lett. 11 (2011) 361-364.

[21] P. Singh, N.Q. Minh, Solid oxide fuel cells: technology status, Int. J. Appl. Ceram. Tec. 1 (2004) 5-15.

[22] K. Zhou, X. Wang, X. Sun, Q. Peng, Y. Li, Enhanced catalytic activity of ceria nanorods from well-defined reactive crystal planes, J. Catal. 229 (2005) 206-212.

[23] X.H. Lu, D.Z. Zheng, J.Y. Gan, Z.Q. Liu, C.L. Liang, P. Liu, Y.X. Tong, Porous CeO_2 nanowires/nanowire arrays: electrochemical synthesis and application in water treatment, J. Mater. Chem. 20 (2010) 7118-7122.

[24] G. Chen, C. Xu, X. Song, W. Zhao, Y. Ding, S. Sun, Interface Reaction Route to Two Different Kinds of CeO_2 Nanotubes, Inorg. Chem. 47 (2008) 723-728.

[25] X. Yang, X. Gao, Y. Gan, C. Gao, X. Zhang, K. Ting, B.M. Wu, Z. Gou, Facile Synthesis of Octacalcium Phosphate Nanobelts: Growth Mechanism and Surface Adsorption Properties, J. Phys. Chem. C 114 (2010) 6265-6271.

[26] F. Meng, C. Zhang, Z. Fan, J. Gong, A. Li, Z. Ding, H. Tang, M. Zhang, G. Wu, Hydrothermal synthesis of hexagonal CeO_2 nanosheets and their room temperature ferromagnetism, J. Alloy Compd. 647 (2015) 1013-1021.

[27] H.L. Bandey, Fingerprint development and imaging newsletter: the powders process, study 1. Sandridge, UK: Police Scientific Development Branch, Home Office, 2004; Report No.:54/04.

[28] S. Shi, M. Hossu, R. Hall, W. Chen, Solution combustion synthesis, photoluminescence and X-ray luminescence of Eu-doped nanoceria CeO_2: Eu, J. Mater. Chem. 22 (2012) 23461–23467.

[29] G.P. Darshan, H.B. Premkumar, H. Nagabhushana, S.C. Sharma, B. Daruka Prasad, S.C. Prashantha, R.B. Basavaraj, Superstructures of doped yttrium aluminates for luminescent and advanced forensic investigations, J. Alloys Compd. 686 (2016) 577 – 587.

[30] H.B. Premkumar, D.V. Sunitha, H. Nagabhushana, S.C. Sharma, B.M. Nagabhushana, C. Shivakumara, J.L. Rao, R.P.S. Chakradhar, Synthesis, characterization, EPR, photo and thermoluminescence properties of $YAlO_3:Ni^{2+}$ nanophosphors, J. Lumin. 135 (2013) 105–112.

[31] R.A. Young, A. Sakthivel, T.S. Moss, C.O. Paiva-Santos, DBWS-9411–an upgrade of the DBWS programs for Rietveld refinement with PC and mainframe computers, J. Appl. Cryst. 28 (1995) 366.

[32] A.A. Jahagirdar, N. Dhananjaya, D.L. Monika, C.R. Kesavulu, H. Nagabhushana, S.C. Sharma, B.M. Nagabhushana, C. Shivakumara, J.L. Rao, R.P.S. Chakradhar, Structural, EPR, optical and magnetic properties of α-Fe_2O_3 nanoparticles, Spectrochim. Acta Part A 104 (2013) 512–518.

[33] F. Meng, C. Zhang, Z.Fan, J. Gong, A. Li, Z. Ding, H.Tang, M. Zhang, G. Wu, Hydrothermal synthesis of hexagonal CeO_2 nanosheets and their room temperature ferromagnetism, J. Alloy Compd. 647 (2015) 1013-1021.

[34] X. Li, J.Li, Di Huo, Z. Xiu, X. Sun, Facile Synthesis under Near-Atmospheric Conditions and Physicochemical Properties of Hairy CeO_2 Nanocrystallines, J. Phys. Chem. C 113 (2009) 1806-1811.

[35] I. Kosacki, V. Petrovsky, H.U. Anderson, P. Colomban, Raman Spectroscopy of Nanocrystalline Ceria and Zirconia Thin Films, Am. Ceram. Soc. Bull 85 (2002) 2646-2650.

[36] L. Ma, D. Wang, J. Li, B. Bai, L. Fu, Y. Li, Ag/CeO_2 nanospheres: Efficient catalysts for formaldehyde oxidation, Appl. Catal. B Environ. 148–149 (2014) 36–43.

[37] L. Minervini, M. O. Zacate, and R. W. Grimes, Defect cluster formation in M_2O_3-doped CeO_2, Solid State Ionics 116(1999) 339-349.

[38] Z.D. Dohcevic-Mitrovic, M. Grujic-Brojcin, M. Scepanovic, Z.V. Popovic, S. Boskovic, B. Matovic, M. Zinkevich, F. Aldinger, $Ce_{1-x}Y$ $(Nd)_xO_{2-\delta}$ nanopowders: potential materials for intermediate temperature solid oxide fuel cells, J. Phys.-Cond. Mat. 18 (2006) S2061-S2068.

[39] H. Gu, M.D. Soucek, Preparation and Characterization of Monodisperse Cerium Oxide Nanoparticles in Hydrocarbon Solvents, Chem. Mater. 19 (2007) 1103-1110.

[40] F. Liang, Y. Yu, W. Zhou, X. Xu, Z. Zhu, Highly defective CeO_2 as a promoter for efficient and stable water oxidation, J. Mater. Chem. A 3 (2015) 634-640.

[41] A.E.C. Palmqvist, M. Wirde, U. Gelius, M. Muhammed, Surfaces of Doped Nanophase cerium oxide Catalysts, Nanostruct. Mater. 11 (1999) 995-1007.

[42] G. Praline, B.E. Koel, R.L. Hance, H.I. Lee, J.M. White, X-Ray Photoelectron Study Of The Reaction Of Oxygen With Cerium, J. Electron. Spectrosc. 21 (1980) 17-30.

[43] G.P. Darshan, H.B. Premkumar, H. Nagabhushana, S.C. Sharma, S.C. Prashantha, H.P. Nagaswarupa, B. Daruka Prasad, Blue light emitting ceramic nano-pigments of Tm^{3+} doped $YAlO_3$: Applications in latent finger print, anti-counterfeiting and porcelain stoneware, Dyes Pigments 131 (2016) 268-281.

[44] M. Venkataravanappa, H. Nagabhushana, B. Daruka Prasad, G.P. Darshan, R.B. Basavaraj, G.R. Vijayakumar, Dual colour emitting Eu doped strontium orthosilicate phosphors synthesized by bio-template assisted ultrasound for solid state lightning and display applications, Ultrason. Sonochem. 34 (2017) 803–820.

[45] N. Sabari Arul, D. Mangalaraj, Pao Chi Chen, N. Ponpandian, C. Viswanathan, Strong quantum confinement effect in nanocrystalline cerium oxide, Mater. Lett. 65 (2011) 2635-2638.

[46] S. Tsunekawa, J. Wang, Y. Kawazoe, A. Kasuya, Blue shifts in the ultraviolet absorption spectra of cerium oxide nanocrystallites, J. Appl. Phys. 94 (2003) 3654.

[47] H. Nakamatsu, T. Mukoyama, H. Adachi, Ionic and covalent bonds in CeO_2 crystal, Chem. Phys. Lett. 247 (1995) 168-172.

[48] S. Tsunekawa, J.T. Wang, Y. Kawazoe, Lattice constants and electron gap energies of nano- and sub nano-sized cerium oxides from the experiments and first-principles calculations, J. Alloy Compd. 408–412 (2006) 1145.

[49] S. Som, A.K. Kunti, Vinod Kumar, Vijay Kumar, S. Dutta, M. Chowdhury, S.K. Sharma, J.J. Terblans, H.C. Swart, Defect correlated fluorescent quenching and electron phonon coupling in the spectral transition of Eu^{3+} in $CaTiO_3$ for red emission in display application, J. Appl. Phys. 115 (2014) 193101-193114.

[50] R.B. Basavaraj, H. Nagabhushana, B. Daruka Prasad, S.C. Sharma, S.C. Prashantha, B.M. Nagabhushana, A single host white light emitting Zn_2SiO_4:Re^{3+} (Eu, Dy, Sm) phosphor for LED applications, Optik. 126 (2015) 1745-1756.

[51] R. Hari Krishna, B.M. Nagabhushana, H. Nagabhushana, R.P.S. Chakradhar, R. Sivaramakrishna, C. Shiva kumara, Tiju Thomas, Auto-ignition based synthesis of Y_2O_3 for photo- and thermo-luminescent applications, J. Alloy Compd. 585 (2014) 129–137.

[52] D.L. Dexter, A Theory of Sensitized Luminescence in Solids, J. Chem. Phys. 21 (1953) 836-850.

[53] Publication CIE no 17.4 International Lighting Vocabulary, Central Bureau of the Commission Internationale de L 'Eclairage, Vienna, Austria, 1987.

[54] Publication CIE no 15.2 Colorimetry, Second Edition, Central Bureau of the Commission Internationale de L 'Eclairage, Vienna, Austria, 1986.

[55] Janos Schanda, M. Danyi, Correlated Color-Temperature Calculations in the CIE 1976 Chromaticity Diagram, Color Res. Appl. 2 (1977)161-163.

[56] S. Som, Subrata Das, S. Dutta, Hendrik G. Visser, Mukesh Kumar Pandey, Pushpendra Kumar, Ritesh Kumar Dubey, S. K. Sharma, Synthesis of strong red emitting Y_2O_3:Eu^{3+} phosphor by potential chemical routes: comparative investigations on the structural evolutions, photometric properties and Judd–Ofelt analysis, RSC Adv. 5 (2015) 70887-70898.

[57] A. Chithambararaj, N. S. Sanjini, S. Velmathi, A. Chandra Bose, Preparation of h-MoO_3 and α-MoO_3 nanocrystals: comparative study on photocatalytic degradation of methylene blue under visible light irradiation, Phys. Chem. Chem. Phys.15 (2013) 14761-14769.

[58] S. Thirumalairajan, K. Girija, N.Y. Hebalkar, D. Mangalaraj, C. Viswanathan, N. Ponpandian, Shape evolution of perovskite $LaFeO_3$ nanostructures: a systematic investigation of growth mechanism, properties and morphology dependent photocatalytic activities, RSC Adv. 3 (2013) 7549–7561.

Authors Bibliography

1. N.H. Deepthi M. Sc.: Physics -2014, Mysore University. Pursuing Ph.D. in Physics, Tumkur University. Presently working as research scholar, Tumkur University, Tumkur – 572 103, India. Area of Interest: Nanomaterials, Luminescence.

2. G. P. Darshan M. Sc.: Physics -2012, Jain University. Pursuing Ph.D. in Physics, Bharathiar University. Presently working as Assistant Professor in the department of Physics, Acharya Institute of Graduate Studies, Bangalore - 560 107, India. Area of Interest: Nanomaterials, Luminescence. Till date: - Citations – 151, H-index- 7 and I-index-7.

3. R. B. Basavaraj M. Sc.: Physics -2012, Gulbarga University. Pursuing Ph.D.in Physics, Tumkur University. Presently working as Junior Research fellow, Tumkur University, Tumkur – 572 103, India. Area of Interest: Nanomaterials, Luminescence. Till date: - Citations – 210, H-index- 10 and I-index-20.

4. Dr. B. Daruka Prasad M.Sc.: Physics – 1998, University of Mysore, Karnataka, India. M.Phil. Physics - 2008, Alagappa University, Tamilnadu, India and Ph.D.: Physics – 2017, JNTUA, Ananthapuramu, Andrapradesh, India. Presently working as assistant Professor at BMS Institute of Technology and Management, Bangalore. Area of Interest: Nanomaterials, Luminescence, Space Science, Photonics etc. Till date: - Citations – 658, H-index- 16 and I-index-28. Guest editor and reviewer for many journals and as an author / co-author published 5 number of books through reputed publishers.

5. Dr. H. Nagabhushana M. Sc.: Physics -1997, Bangalore University, Bangalore, Karnataka, India. M. Phil.: Physics - 2000, Bangalore University. Ph.D.: Solid state Physics - 2002, Bangalore University, D. Sc.: in Materials Science, Tumkur University, Tumkur, Karnataka, India, Bangalore University. Presently working as Professor and Head of the Department, Prof. C N R Rao Centre for Advanced Materials, Tumkur University, Tumkur - 572103, India. Area of Interest: Nanomaterials, Luminescence, defects studies, SHI irradiation, Space Science, etc. Till date: -Citations –3341, H-index- 29 and I-index-124. Reviewer for many journals and published many number of book / book chapters through reputed Publishers.

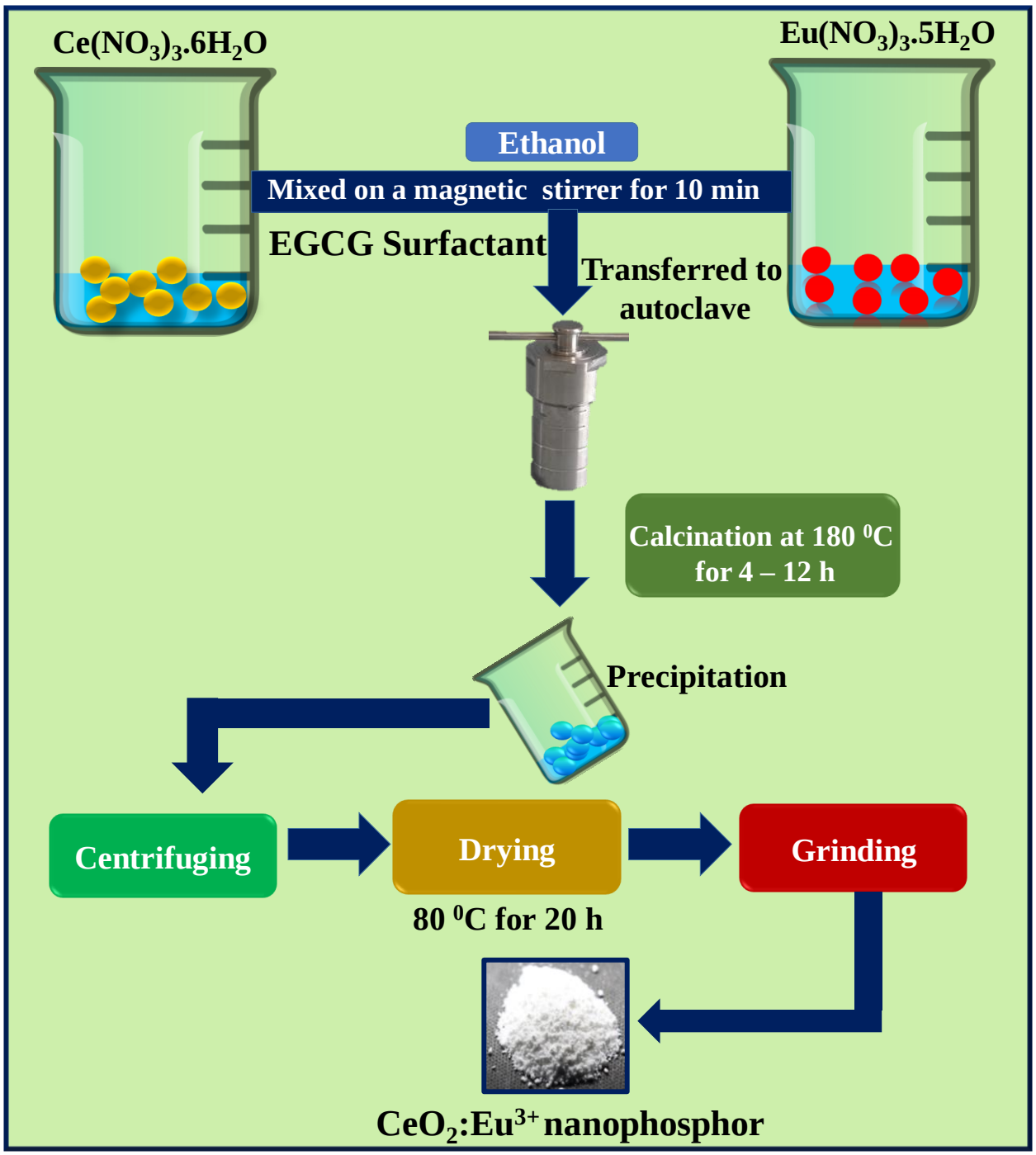

Fig.1. Schematic representation of hydrothermal synthesis of Eu^{3+} doped CeO_2 NP using EGCG surfactant.

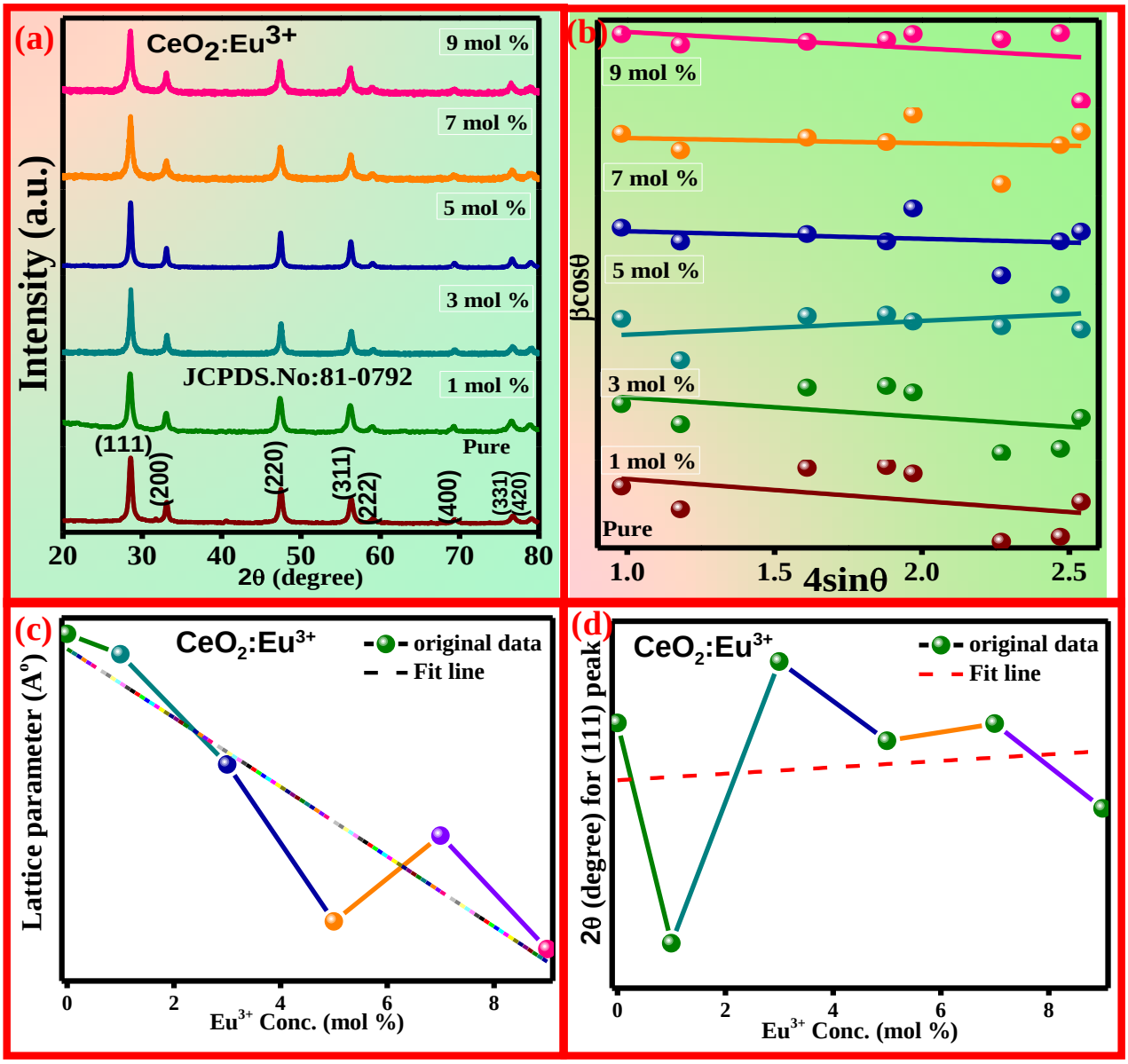

Fig.2 (a) PXRD patterns, (b) W-H plots, and (c & d) lattice parameter and 2θ for (111) peak position as a function of Eu^{3+} concentration in pure and CeO_2:Eu^{3+} (1-9 mol %) NP synthesized with 180 °C and 30 %W/V of *EGCG* for 12 h.

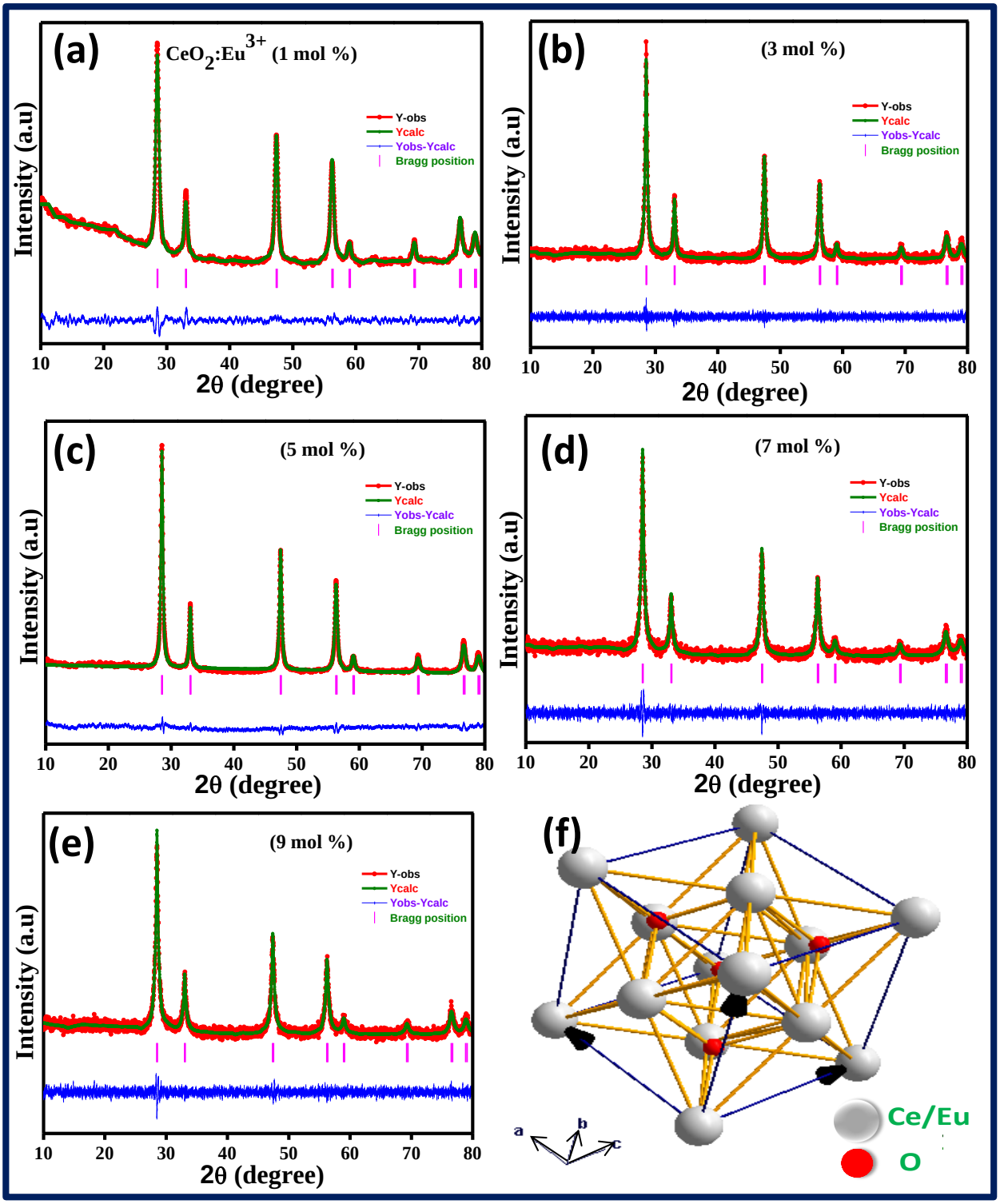

Fig.3 (a-e) Rietveld refinement and (f) packing diagram of $CeO_2:Eu^{3+}$ (3 mol %) NP.

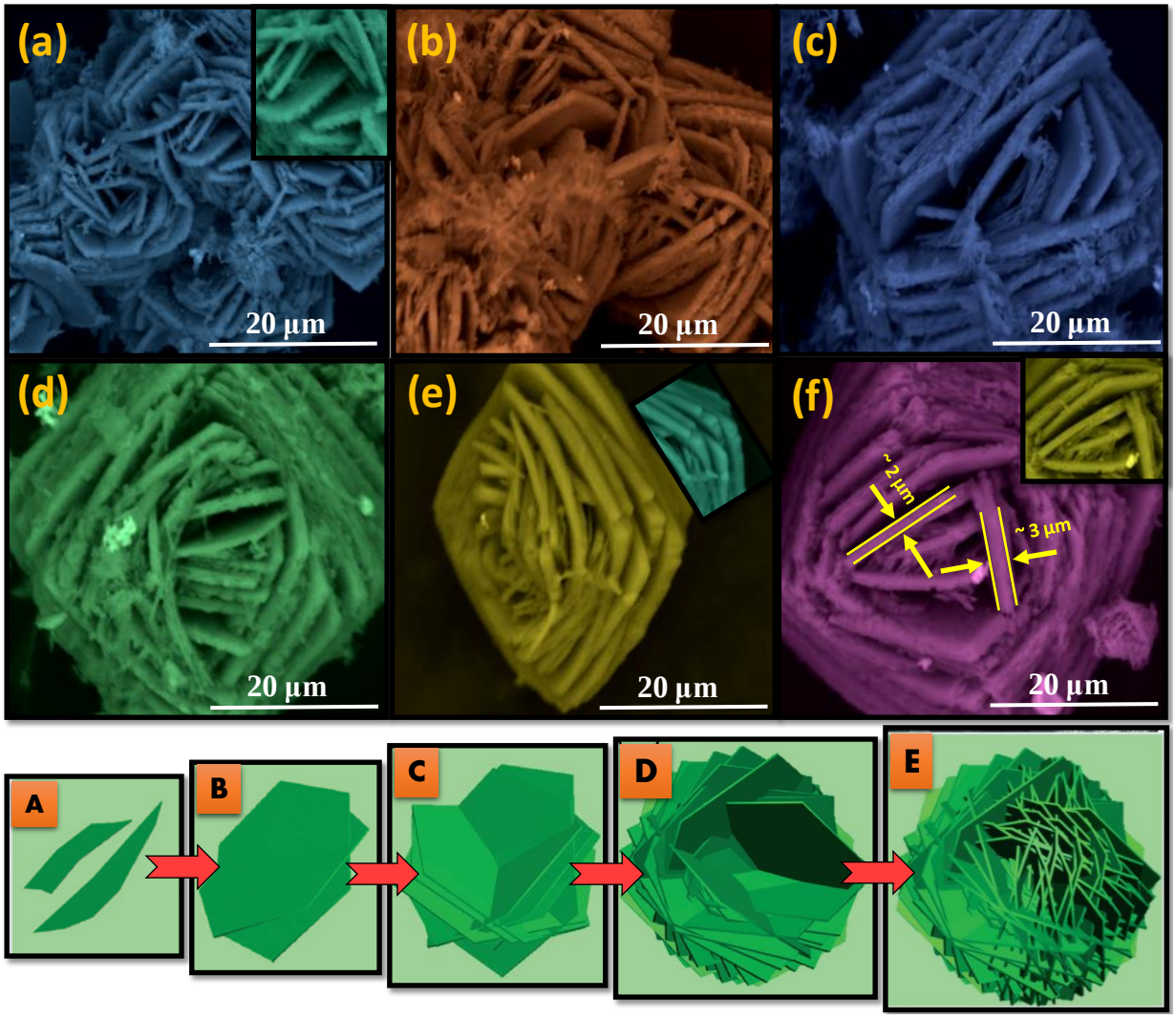

Fig.4. SEM images of $CeO_2:Eu^{3+}$ (3 mol %) NP prepared with different reaction time (a) 2, (b) 4, (c) 6, (d) 8, (e) 10 and (f) 12 h with 30 %W/V of *EGCG* at 180 ^{o}C and (A-E) depicts probable growth mechanism of 3D hierarchical flower-like architecture.

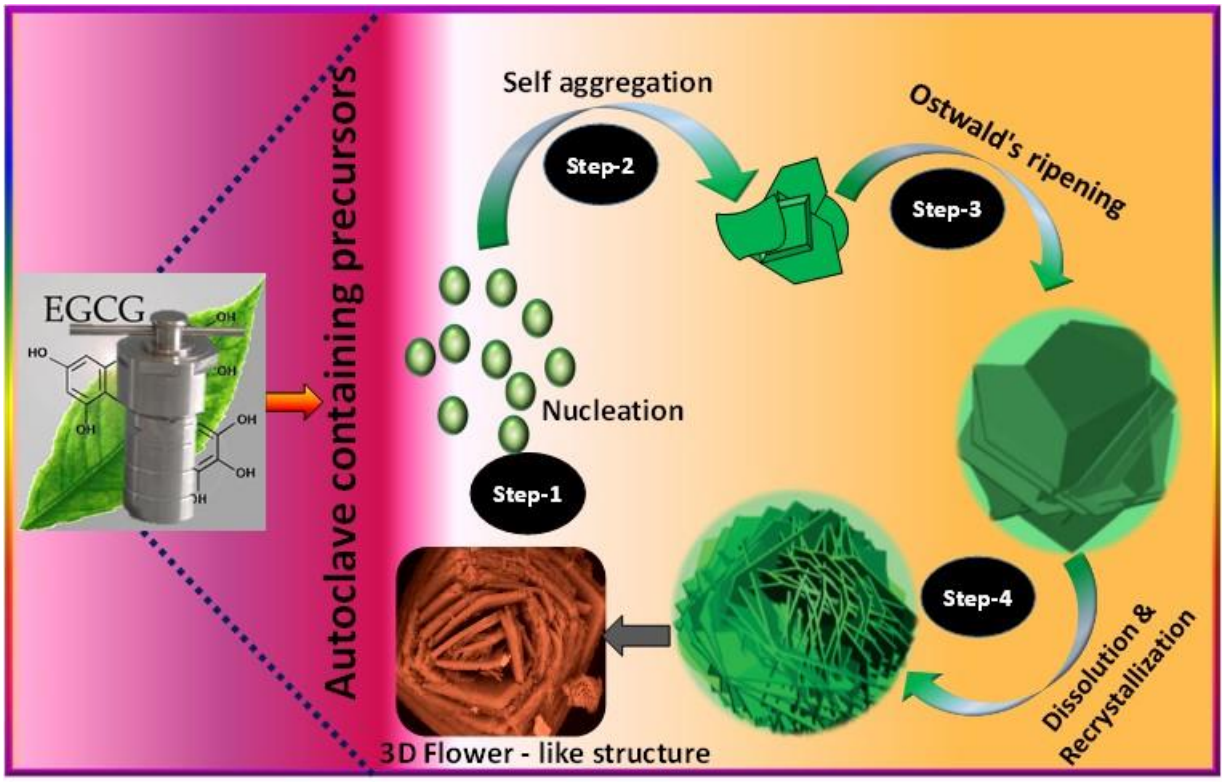

Fig.5. Schematic representation of growth mechanism involving nucleation, self - aggregation, Ostwald's ripening dissolution and recrystallization.

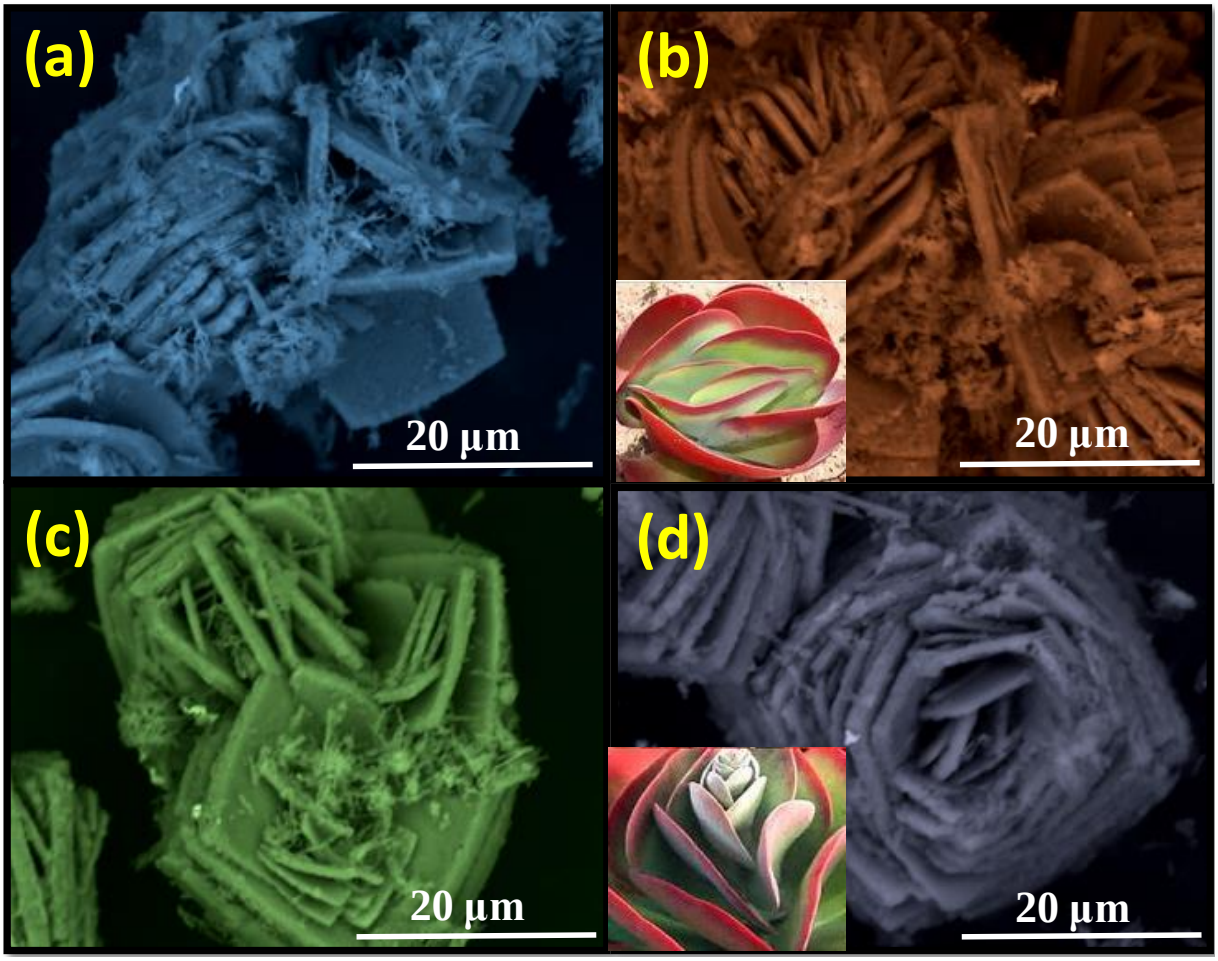

Fig.6. SEM images of $CeO_2:Eu^{3+}$ (3 mol %) NP prepared with different concentration of EGCG (a) 5, (b) 10, (c) 20 and (d) 30 %W/V while reaction temperature and time are fixed at 180 ^oC and 12 h respectively.

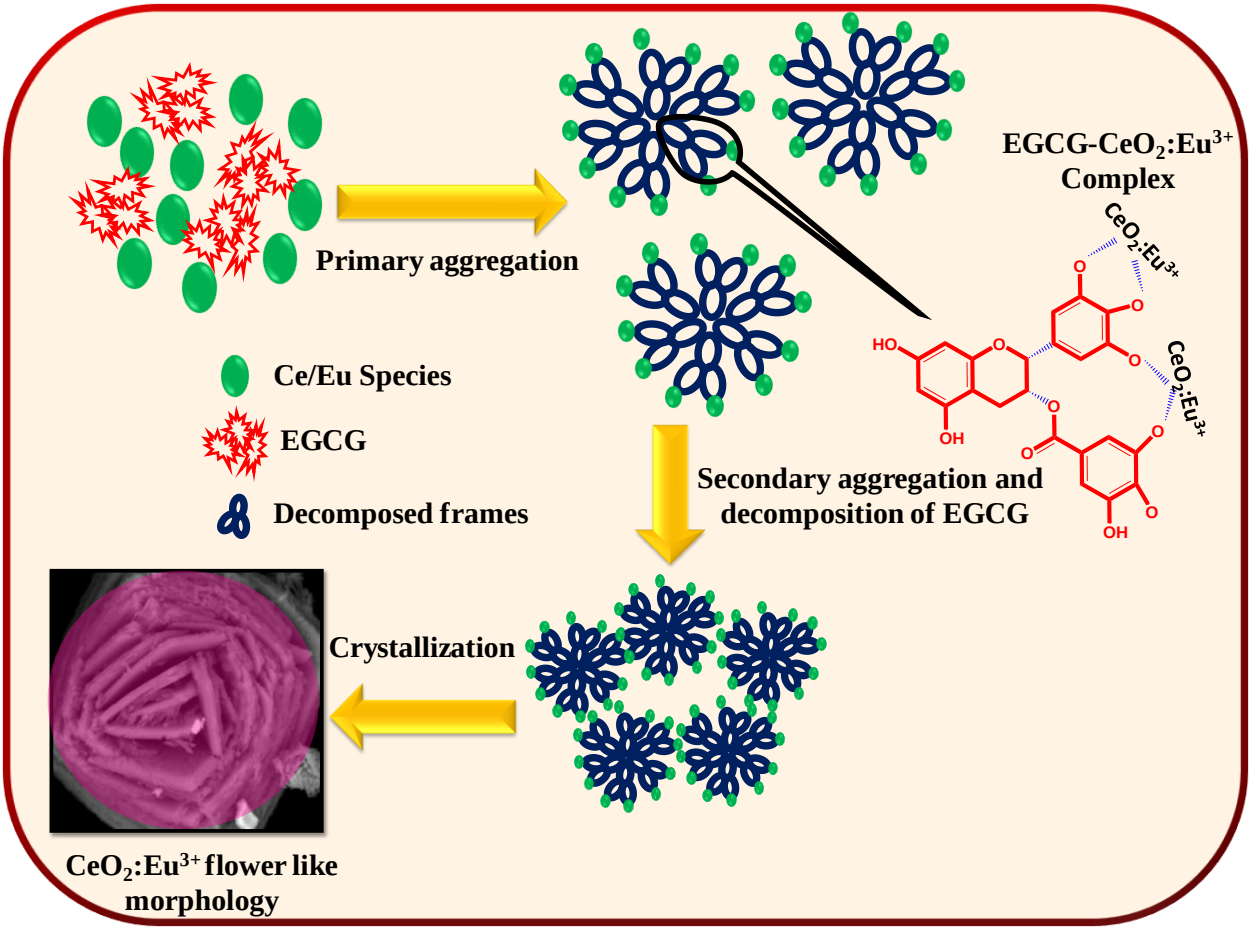

Fig.7. Probable mechanism for the growth of 3D flower - like morphology of $CeO_2:Eu^{3+}$ (3 mol %) NP in the presence of EGCG surfactant.

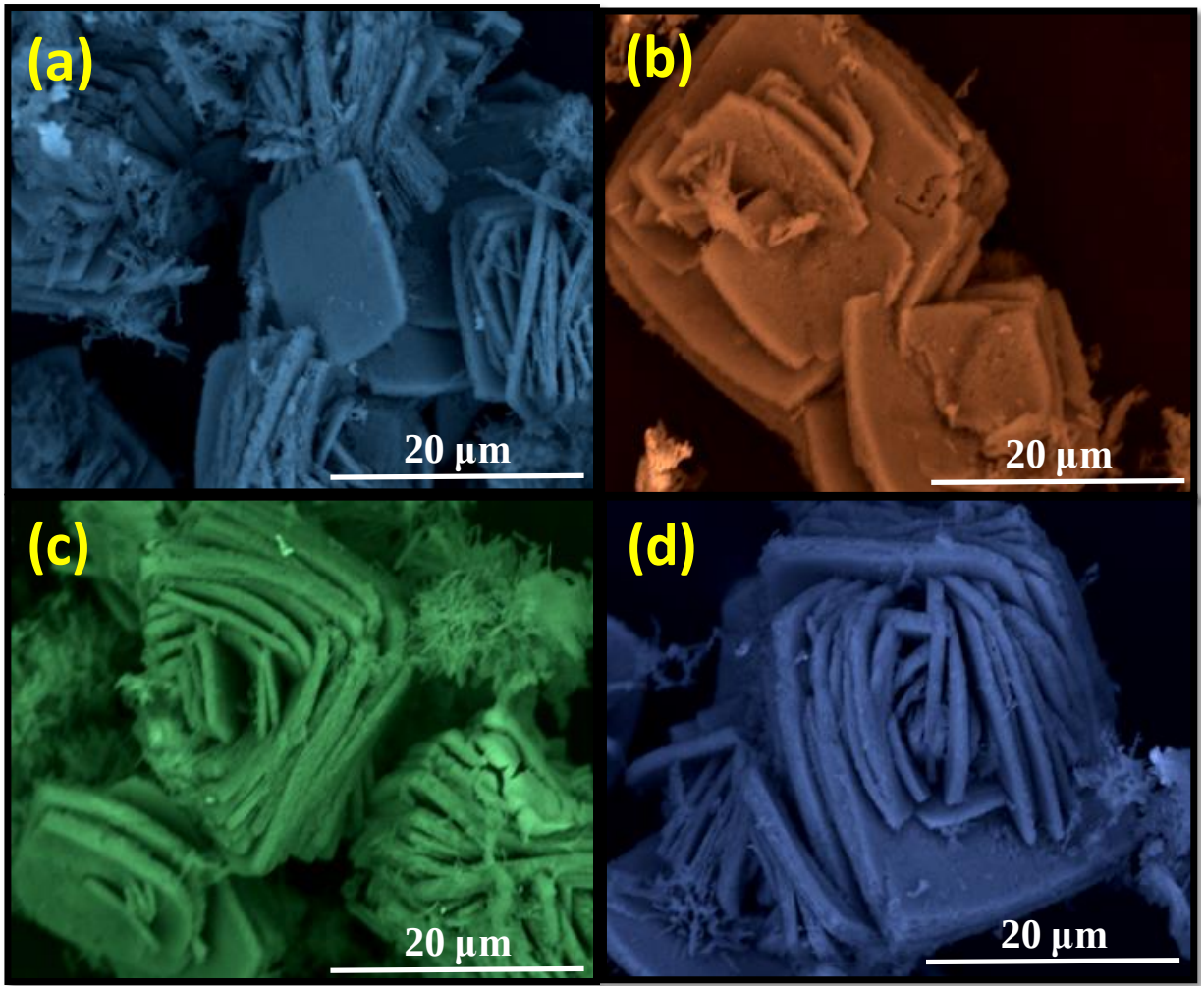

Fig.8. SEM micrographs of CeO_2:Eu^{3+} (3 mol %) NP prepared with different synthesis temperature (120 -180 ºC) using 30 %W/V of EGCG for 12 h.

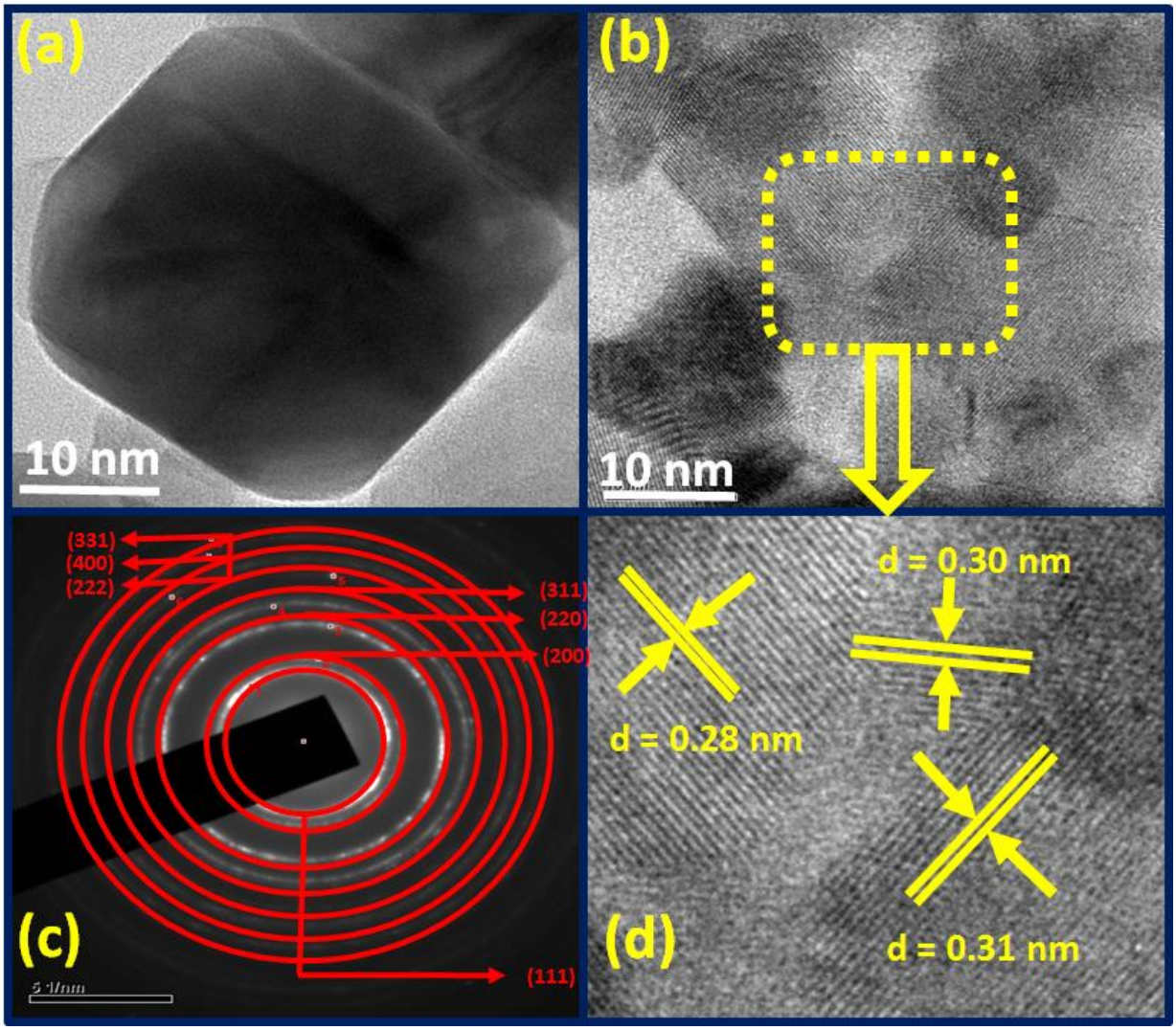

Fig.9 (a) TEM, (b) HRTEM image, (c) SAED patterns and (d) magnified view of HRTEM image of CeO_2:Eu^{3+} (3 mol %) NP prepared with EGCG (30 %W/V) at 180 ^oC for 12 h.

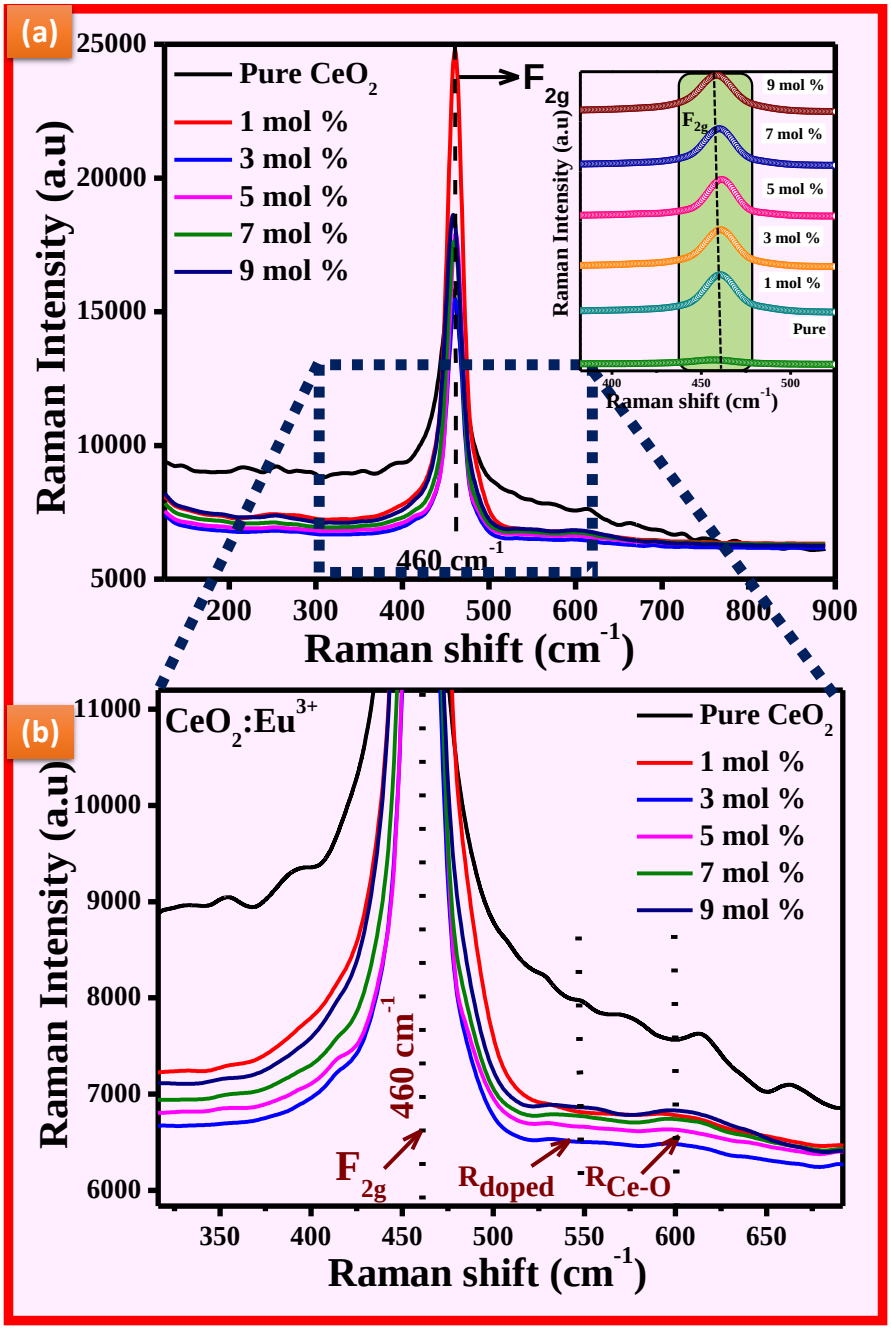

Fig.10 (a) Raman spectra of pure and CeO_2:Eu^{3+} (1-9 mol %) NP and (b) Enlarged portion of the spectra.

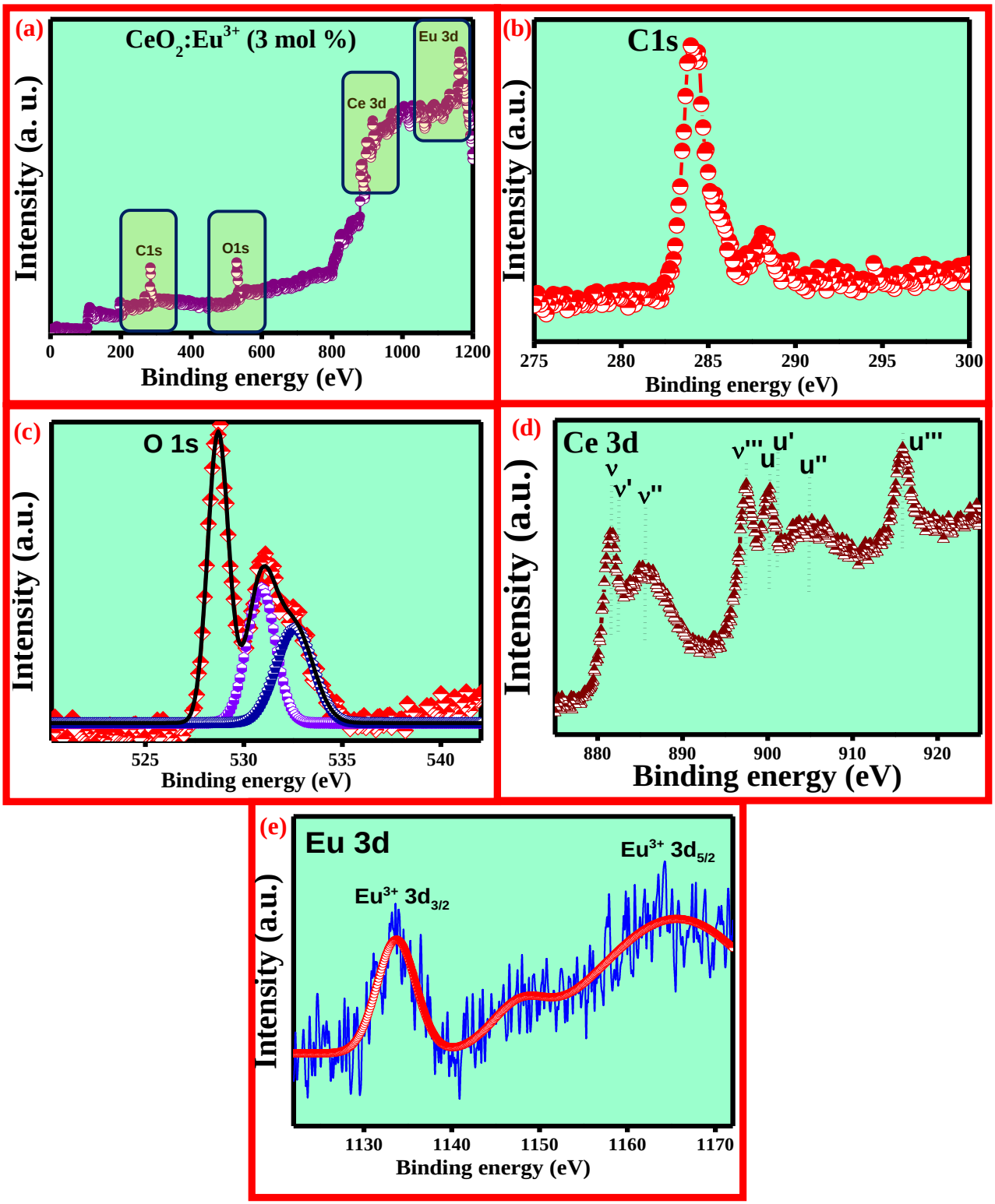

Fig.11(a) Wide scanning XPS spectrum of CeO_2:Eu^{3+} (3 mol %) NP and high-solution XPS spectrum of (b) C1s, (c) O 1s, (d) Ce 3d and (e) Eu 3d.

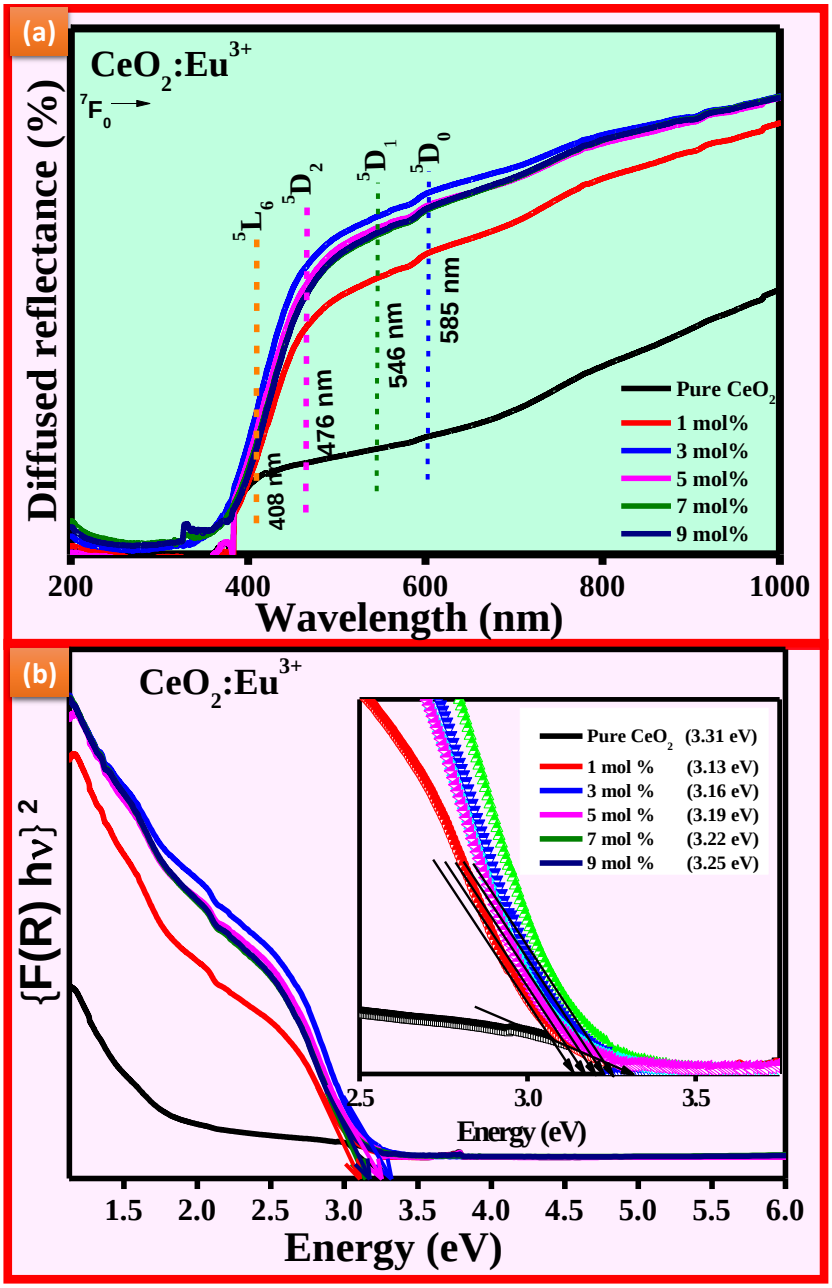

Fig.12 (a) DR spectra and (b) Energy band gap of CeO_2:Eu^{3+} (1-9 mol %) NP.

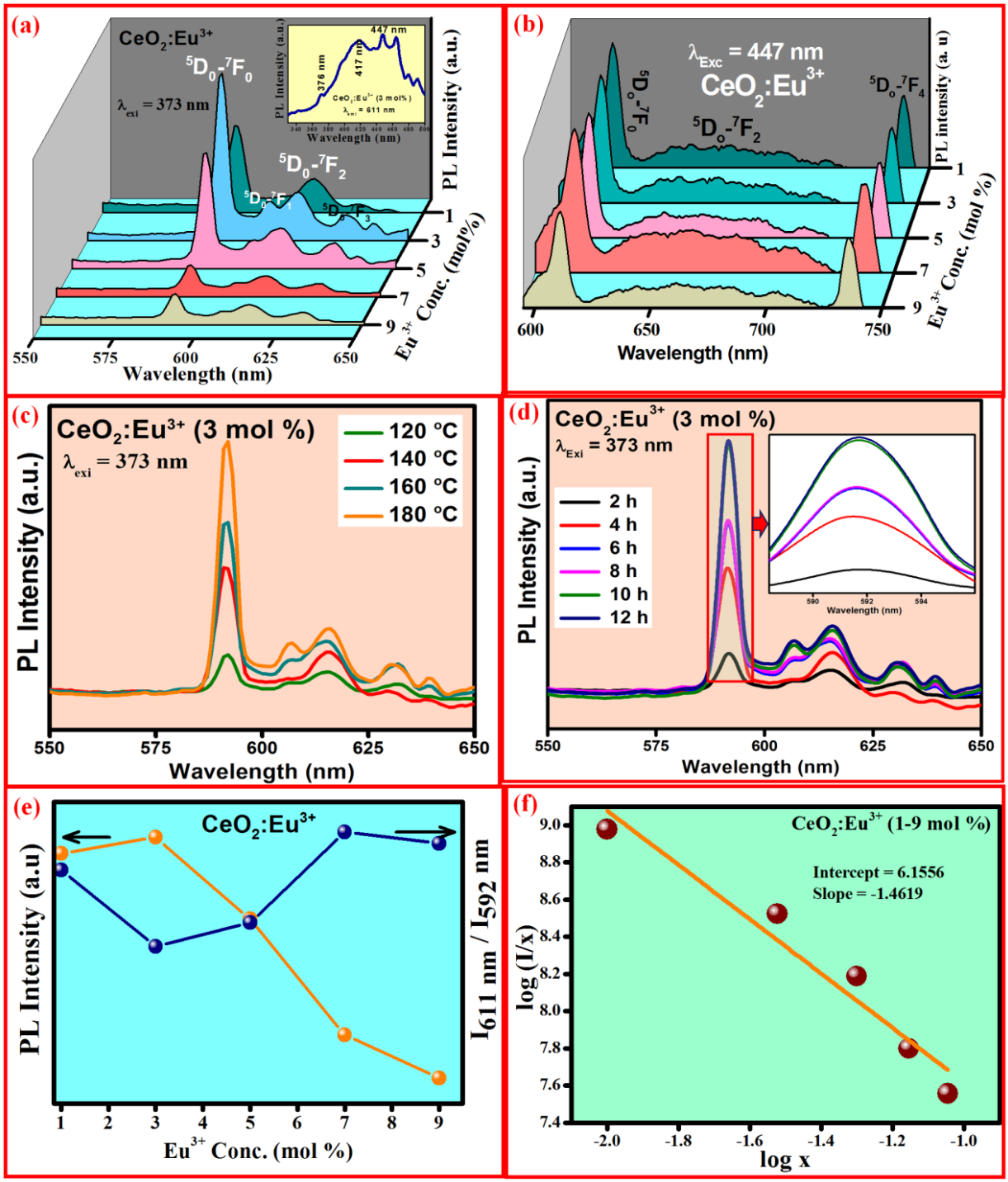

Fig.13(a & b) PL Emission spectra of $CeO_2:Eu^{3+}$ (3 mol %) NP excited at 373 and 447 nm (Inset: Excitation spectra), (c & d) PLE spectra of $CeO_2:Eu^{3+}$ (3 mol %) NP synthesized with different temperature and reaction time respectively, (e) PL emission intensity and asymmetric ratio as a function of Eu^{3+} ion concentration and (f) logarithmic plot of (x) versus (I/x) of $CeO_2:Eu^{3+}$ (1-9 mol %) NP synthesized at 180 ^oC for 12 h with 30 %W/V EGCG.

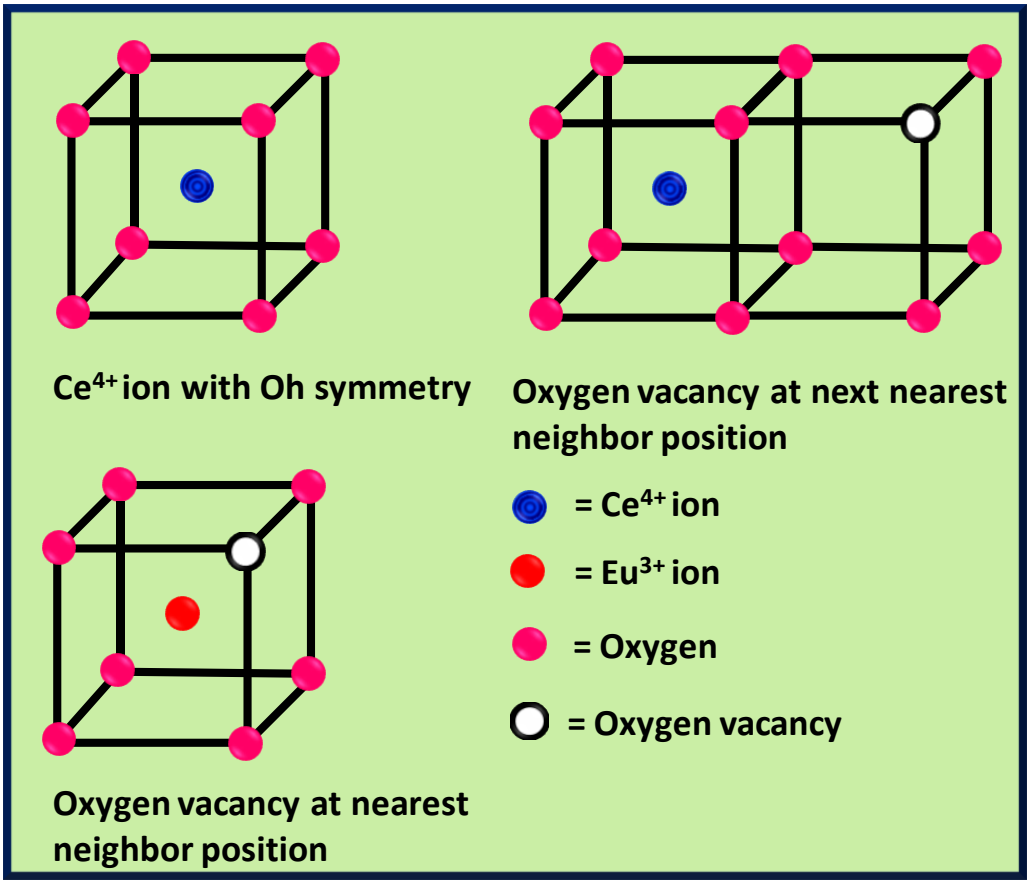

Fig.14.Schematic representation of creation of oxygen vacancy in CeO_2:Eu^{3+} NP.

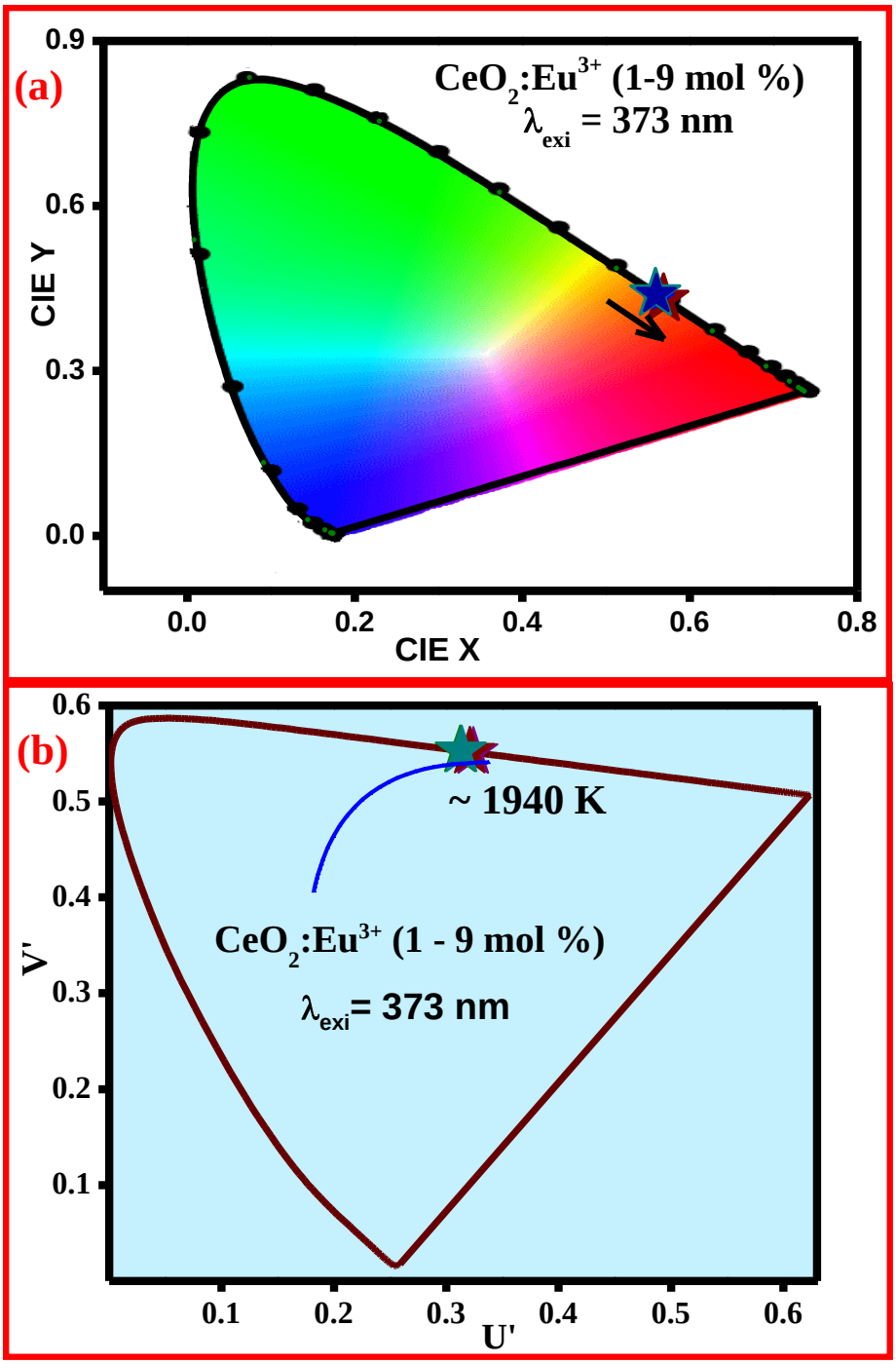

Fig.15 (a) CIE and (b) CCT diagram of $CeO_2:Eu^{3+}$ (1-9 mol %) NP excited at 373 nm.

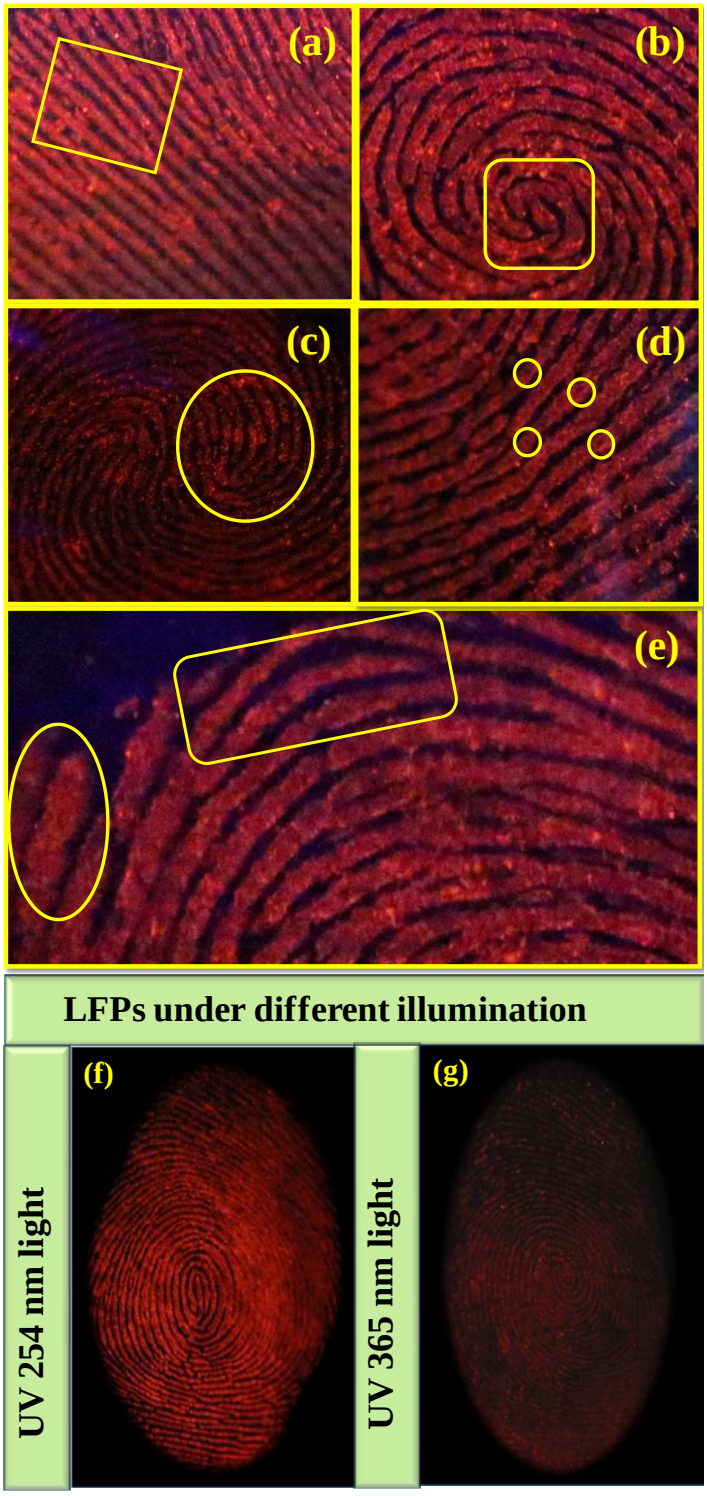

Fig.16. Post processed LFPs visualized by $CeO_2:Eu^{3+}$ (3 mol %) NP on glass under 254 nm light which exhibits (a) bifurcation, (b) whorl, (c) loop, (d) island, (e) lake and (f & g) LFPs visualized under different illumination light.

Fig.17. LFPs visualized by $CeO_2:Eu^{3+}$ (3 mol %) NP on (a & b) aluminum foil (c & d) stainless steel, (e & f) plastic sheet, (g & h) wooden floor sheet and (i & j) compact disk cover under normal visible and UV 254 nm light respectively.

Fig.18(a-f) LFPs visualized by $CeO_2:Eu^{3+}$ (3 mol %) NP on various surfaces of paper substrates with different background colors.

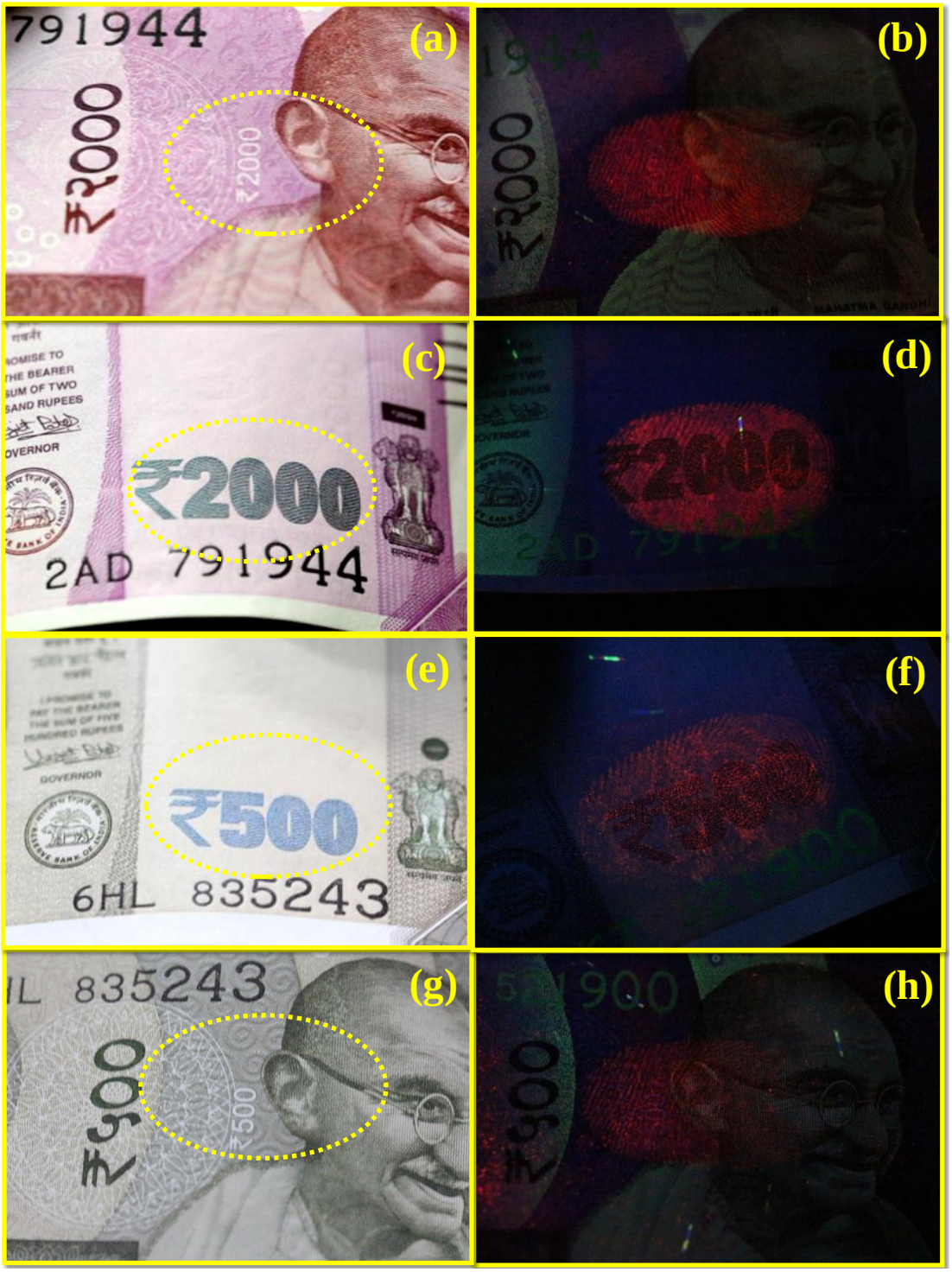

Fig.19. LFPs visualized by staining CeO_2:Eu^{3+} (3 mol %) NP on the various portion of Indian currency under (a, c, e and g) visible light and (b, d, f and h) UV 254 nm light.

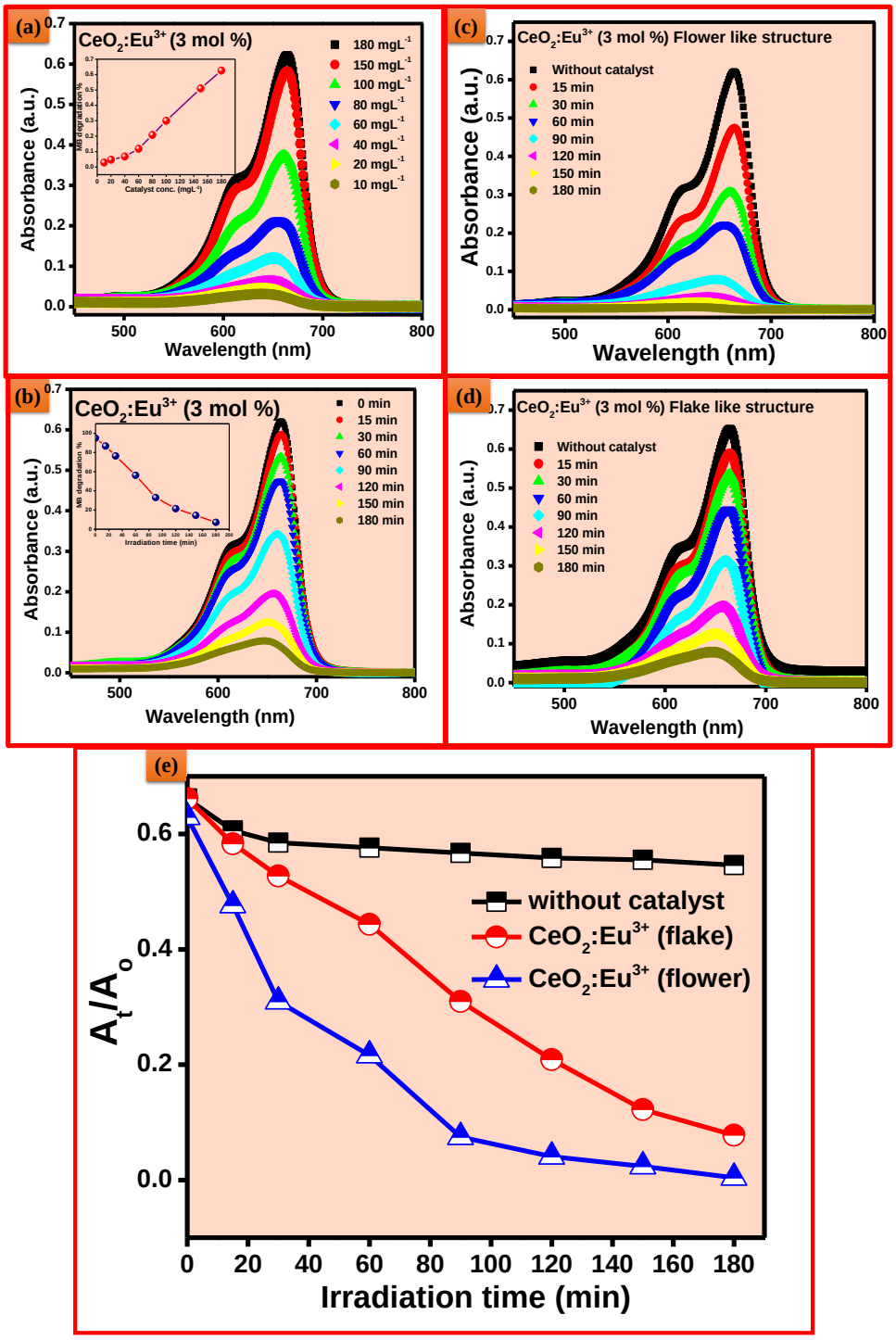

Fig.20. UV-Vis spectra of MB degradation using $CeO_2:Eu^{3+}$ (3 mol %) NP with (a) concentration of catalyst and (b) time period (insets MB degradation %), (c & d) MB degradation of flake and flower morphologies and (e) degradation trend of MB as a function of irradiation time in the presence of flake and flower like morphologies of $CeO_2:Eu^{3+}$ NP.

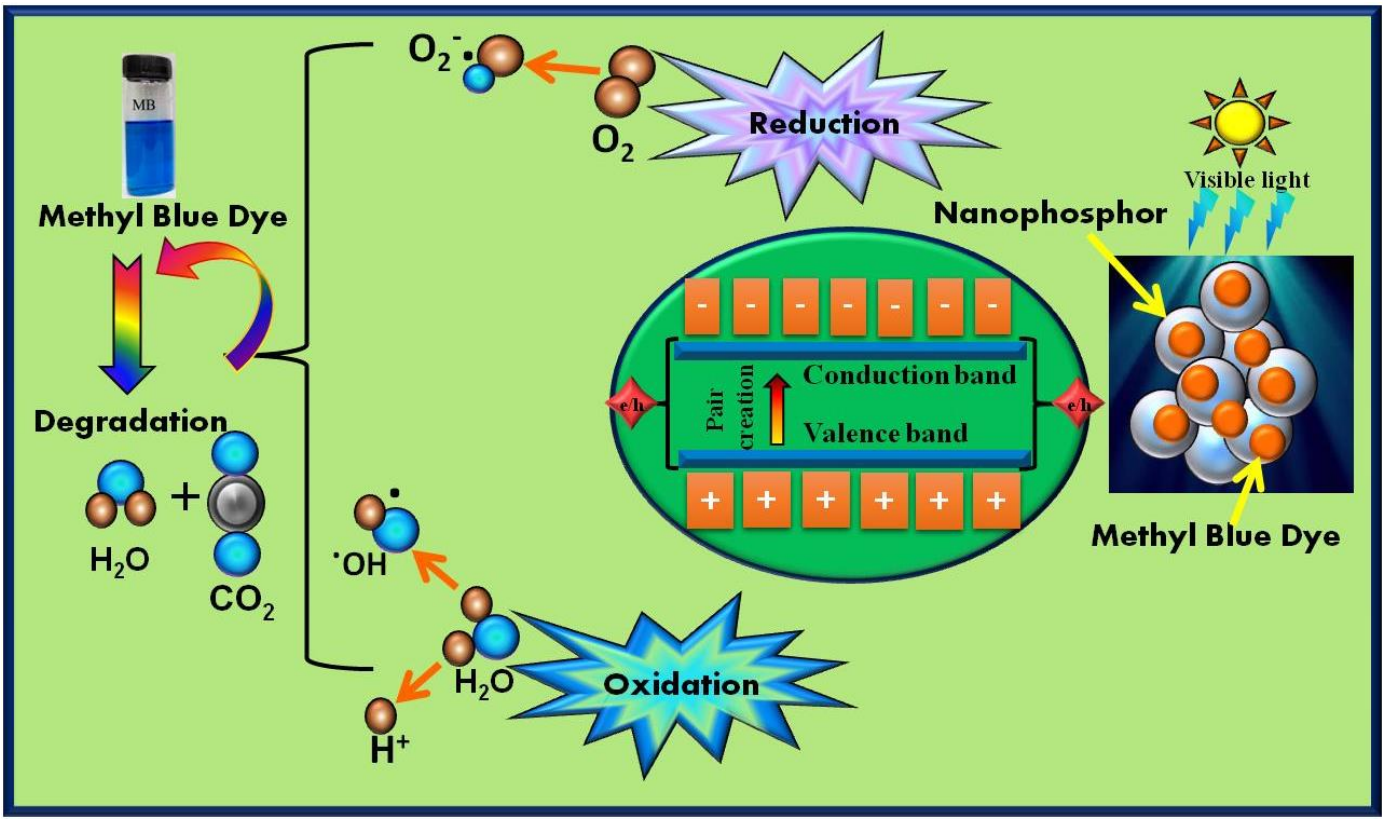

Fig.21. Schematic diagram of photocatalytic activity of the optimized CeO_2:Eu^{3+} (3 mol %) NP on MB dye under visible light irradiation.

Table.1. Bandey FP grading scheme.

Grade	Description
0	No description
1	No continuous ridges; all discontinuous or dotty
2	One third of the mark comprised of continuous ridges; remainder either show no development or dotty
3	Two thirds of the mark comprised of continuous ridges; remainder either show no development or dotty
4	Full development; whole mark comprised of continuous ridges

Table.2. Estimated crystallite size, lattice strain, stacking fault, dislocation density and band gap energy of pure and Eu^{3+} (1-9 mol %) doped CeO_2 NP.

Eu^{3+} (mol %)	**Average crystallite size D (nm)**		**Strain Ɛ ($x10^{-3}$)**	**Stacking fault (mJm^{-2})**	**Dislocation density δ $x10^{15}$ (m^{-2})**	**Energy Band gap (eV)**
	Scherrer's method	**W-H Plots**				
Pure	13	26	4.03	0.45	5.90	3.31
1	8	11	3.26	0.49	12.82	3.13
3	11	32	5.53	0.47	7.48	3.16
5	12	23	4.12	0.45	5.68	3.19
7	11	36	5.69	0.44	7.53	3.22
9	8	20	4.56	0.43	12.5	3.25

Table.3.Rietveld refinement parameters of CeO_2:Eu^{3+} (1-9 mol %) NP.

Rietveld refined structural parameters (JCPDF No:34-394)					
Compound	**1 mol %**	**3 mol %**	**5 mol %**	**7 mol %**	**9 mol %**
Crystal system			Cubic		
Space group			Fm-3m (225)		
Lattice parameters (Å)					
a=b=c	5.4222	5.4169	5.4181	5.4188	5.4234
α=β=γ	90°	90°	90°	90°	90°
Unit cell volume ($Å^3$)	159.4108	158.9437	159.0552	159.1152	159.5173
Refinement parameters					
R_P	2.33	5.34	3.65	5.53	5.51
R_{WP}	2.99	6.82	4.53	6.93	6.84
R_{Exp}	8.75	6.43	6.70	6.53	6.34
χ^2	0.116	1.13	0.45	1.13	1.16
GoF	0.34	1.00	0.67	1.00	1.10
R_{Bragg}	1.61	2.28	13.2	2.54	2.58
R_F	1.25	1.84	8.84	1.96	2.00
X-ray density (g/cc^3)	7.172	7.199	7.293	7.228	7.161

Table.4. Estimated Oxygen vacancy values compared with lattice parameter of the pure and CeO_2:Eu^{3+} (1-9 mol %) NP.

Eu^{3+} Conc. (mol %)	**Lattice parameter (Å)**	**R_{wp}**	**Area Oxygen vacancies/area of F_{2g} (%)**
Pure	5.42	15.01	12.80
1	5.42	14.56	11.43
3	5.41	13.28	07.97
5	5.40	12.34	08.98
7	5.41	13.11	11.24
9	5.40	12.60	11.60

Table.5. Photometric characteristics of CeO_2: Eu^{3+} (1-9 mol %) NP.

Eu^{3+} Conc. (mol %)	**CIE**		**CCT (K)**	**CP (%)**	**QE (%)**
	X	**Y**			
1	0.5591	0.4398	1975	80.35	68
3	0.5688	0.4301	1880	84.32	84
5	0.5665	0.4325	1902	82.15	78
7	0.5590	0.4399	1976	79.46	74
9	0.5603	0.4386	1962	78.42	79